

PEGylated Anionic Magneto-Fluorescent Nanoassemblies: Impact of their Interface Structure on MRI Contrast and Cellular Uptake

Camille Linot, Julien Poly, Joanna Boucard, Daniel Pouliquen, Steven Nedellec, Philippe Hulin, Nadège Marec, Paolo Arosio, Alessandro Lascialfari, Andrea Guerrini, et al.

▶ **To cite this version:**

Camille Linot, Julien Poly, Joanna Boucard, Daniel Pouliquen, Steven Nedellec, et al.. PEGylated Anionic Magneto-Fluorescent Nanoassemblies: Impact of their Interface Structure on MRI Contrast and Cellular Uptake. ACS Applied Materials & Interfaces, 2017, 9 (16), pp.14242-14257. 10.1021/acsami.7b01737 . inserm-01522631

HAL Id: inserm-01522631

https://inserm.hal.science/inserm-01522631

Submitted on 15 May 2017

HAL is a multi-disciplinary open access archive for the deposit and dissemination of scientific research documents, whether they are published or not. The documents may come from teaching and research institutions in France or abroad, or from public or private research centers.

L'archive ouverte pluridisciplinaire **HAL**, est destinée au dépôt et à la diffusion de documents scientifiques de niveau recherche, publiés ou non, émanant des établissements d'enseignement et de recherche français ou étrangers, des laboratoires publics ou privés.



PEGylated Anionic Magneto-Fluorescent Nanoassemblies: Impact of their Interface Structure on MRI Contrast and Cellular Uptake

Camille Linot, Julien Poly, Joanna Boucard, Daniel Pouliquen, Steven Nedellec, Philippe Hulin, Nadège Marec, Paolo Arosio, Alessandro Lascialfari, Andrea Guerrini, et al.

▶ **To cite this version:**

Camille Linot, Julien Poly, Joanna Boucard, Daniel Pouliquen, Steven Nedellec, et al.. PEGylated Anionic Magneto-Fluorescent Nanoassemblies: Impact of their Interface Structure on MRI Contrast and Cellular Uptake. ACS Applied Materials & Interfaces, American Chemical Society, 2017, .

HAL Id: inserm-01522631

http://www.hal.inserm.fr/inserm-01522631

Submitted on 15 May 2017

HAL is a multi-disciplinary open access archive for the deposit and dissemination of scientific research documents, whether they are published or not. The documents may come from teaching and research institutions in France or abroad, or from public or private research centers.

L'archive ouverte pluridisciplinaire **HAL**, est destinée au dépôt et à la diffusion de documents scientifiques de niveau recherche, publiés ou non, émanant des établissements d'enseignement et de recherche français ou étrangers, des laboratoires publics ou privés.

PEGylated Anionic Magneto-Fluorescent Nanoassemblies: Impact of their Interface Structure on MRI Contrast and Cellular Uptake

Camille Linot,[†] Julien Poly,[‡] Joanna Boucard,[§] Daniel Pouliquen,[†] Steven Nedellec,[≠] Philippe Hulin,[≠] Nadège Marec,[#] Paolo Arosio, [⊥]Alessandro Lascialfari,[⊥Δ] Andrea Guerrini,[//] Claudio Sangregorio,[//] Marc Lecouvey,[⊥] ,[‡] Lénaïc Lartigue,[§] Christophe Blanquart,*[†] and Eléna Ishow*[§]*

[†]CRCINA, INSERM, Université d'Angers, Université de Nantes, Nantes. [‡]IS2M–UMR CNRS 7361, Université de Haute-Alsace, 15 rue Jean Starcky, 68057 Mulhouse, France. [§]CEISAM–UMR CNRS 6230, Université de Nantes, 2 rue de la Houssinière, 44322 Nantes, France. [≠]INSERM UMS 016-UMS CNRS 3556, 8 quai Moncousu, 44007 Nantes, France. [#]Plateforme CytoCell, INSERM UMR 1232, Nantes, France. [⊥]Department of Physics, Università di Pavia, via Bassi, 27100 Pavia, Italy. [Δ]Department of Physics, Università degli Studi di Milano and INSTM, via Celoria 16, 20133 Milano, Italy. [‖]ICCOM-CNR, via Madonna del Piano 10, 50019 Sesto Fiorentino, FI, Italy. [⊥]CSPBAT-UMR CNRS 7244, Université de Villetaneuse – Paris 13, 74 rue Marcel Cachin, 93017 Bobigny, France.

KEYWORDS. Multimodal nanoassemblies, organic nanoparticles, iron oxide nanoparticles water-soluble RAFT polymers, fluorescence, MRI, live cells, spheroids.

ABSTRACT. Controlling the interactions of functional nanostructures with water and biological media represents high challenges in the field of bioimaging applications. Large contrast at low doses, high colloidal stability in physiological conditions, absence of cell cytotoxicity and efficient cell internalization represent strong additional needs. To achieve such requirements, we report on high payload magneto-fluorescent architectures, made of a shell of superparamagnetic iron oxide nanoparticles tightly anchored around fluorescent organic nanoparticles. Their external coating is simply modulated using anionic polyelectrolytes in a final step to provide efficient MRI and fluorescence imaging of live cells. Various structures of pegylated polyelectrolytes have been synthesized and investigated, differing from their iron oxide complexing units (carboxylic versus phosphonic acid), their structure (block or comb-like), their hydrophobicity and their fabrication process (conventional or RAFT-controlled radical polymerization) while keeping the central magneto-fluorescent platforms the same. Combined photophysical, magnetic, NMRD and structural investigations proved the superiority of RAFT polymer coatings containing carboxylate units and a hydrophobic tail to impart the magnetic nanoassemblies with enhanced-MRI negative contrast, characterized by a high r_2/r_1 ratio and transverse relaxation r_2 equal to 21 and 125 $s^{-1}mmol^{-1}L$ respectively at 60 MHz clinical frequency (~1.5 T). Thanks to their dual modality, cell internalization of the nanoassemblies in mesothelioma cancer cells could be evidenced both by confocal fluorescence microscopy and magnetophoresis. A 72 h follow-up showed efficient uptake after 24 h with no notable cell mortality. These studies again pointed out the distinct behavior of RAFT polyelectrolyte-coated bimodal nanoassemblies that internalize at a slower rate with no adverse cytotoxicity. Extension to multicellular tumor cell spheroids that mimic solid tumors revealed successful internalization of the nanoassemblies in the periphery cells, which provides efficient deep-imaging labels thanks

to their induced T_2* contrast, large emission Stokes shift and bright dot-like signal, popping out of the strong spheroid autofluorescence.

INTRODUCTION

Multifunctional nanoassemblies comprising units with complementary properties have emerged as must-have systems in the field of bioimaging for the last decade.[1-2] They advantageously enable cross-correlation analyses to avoid false positives and adapt more easily to the location or the target to be examined, opening the path toward personalized medicine. In this respect, magneto-fluorescent nanostructures represent attractive multimodal imaging agents that can bridge the gap between *in vitro* and *in vivo* investigations. They facilitate high-resolution diagnosis under simple handling and addressing conditions without requiring specific protection equipment against ionizing radiation.[3-4] Designing complex architectures with high performances thus represents one big challenge while colloidal and chemical stability, biodegradability as well as non-significant toxicity represent even higher stakes. For these reasons, superparamagnetic iron oxide nanoparticles (SPIONs), regarded as non-cytotoxic,[5] have widely been used as efficient negative contrast agents in magnetic resonance imaging (MRI) thanks to their large transverse relaxivity r_2, and their possible biodegradation upon mineralization and sequestration in iron-loading and transferring proteins.[6-7] Small superparamagnetic magnetite Fe_3O_4 or maghemite γ-Fe_2O_3 nanoparticles with diameter less than 10 nm have attracted special attention as they are faster cleared *in vivo* compared to larger nanoparticles.[8-10] To provide higher imaging contrast, recent interest has been paid to tight clustering of SPIONs within single nanoassemblies of larger sizes, so that high magnetic field inhomogeneity is produced, speeding up transverse

relaxation of the surrounding water protons due to strong spin dephasing.[3,10-14] Cross-linked silica or latex matrices have been much praised in the past to encapsulate fluorescent and magnetic units. Owing to their poor biodegradability capabilities, they are nowadays being supplanted by hydrophilic polymers and liposomes that simply entrap functional units upon phase demixing and offer potential clinical transfer.[15-16] However, the later associations face one main drawback, relying on the absence of specific interactions between the stabilizing chains/shells and the assembled iron oxide nanoparticles. Uncontrolled progressive release of SPIONs can occur due to natural liposome rupture or small ion decomplexation, hence steric or charge repulsions are lost and lead to deleterious nanoparticle agglomeration and reduced contrast efficiency. Seeking for stable associations with a high magnetic contrast while keeping hydrodynamic diameters less than 200 nm large thus represent high challenges. Such nanoassemblies were fabricated in nitric acid, which precluded any further biological use.[17] We thus resorted to polyelectrolytes such as poly(acrylic acid) (PAA), containing strong iron oxide chelating units, to stabilize the outer surface of the core-shell structures in water. By contrast, small citrate ions revealed to be unable to ensure tight cohesion of the whole structure *in vitro* and conducted to progressive dissembling of the magnetic nanoparticles and fluorescent core.[18] Thus, PAA has currently appeared as a very attractive biocompatible stabilizing ligand as it displays strong affinity for iron oxide,[19-20] little toxicity[21] and multiple anchoring points, limiting its detachment from the iron oxide surface, even after *in vivo* injection.[22] More recently, poly(phosphonic acid) (PPA) known for its even larger association to iron, was also showed to form very strong stabilizing shell around SPIONs.[23-24] While most of studies have largely investigated the impact of the diameter of SPIONs and magnetic nanoassemblies on MRI contrast and cellular uptake,[5,25] the effects of the polymer shell architecture are much more rarely

been scrutinized.[26-27] And yet, evidence has been reported on the consequences of gold nanoparticle surface structuration (regular versus irregular) with molecular brushes[25,28] onto the membrane penetration mechanism while polymer geometries (cyclic *versus* linear) of polyester nanocarriers influence the pharmacokinetics of drug delivery.[29]

In order to focus on the impact of the polymer architectures, regardless of the length of the polymer main chain and the shape of the nanoassemblies (NAs), we have targeted biocompatible hydrophilic polymers, differing only by their geometry, their hydrophobicity and chelating strength of SPIONs to stabilize the outer surface of high-density magneto-fluorescent architectures in water and physiological media. Since pegylation offers limited protein adsorption and additional increased blood circulation time for further *in vivo* investigations,[8,30] three distinct architectures containing poly(ethylene glycol) (PEG) chains were explored, varying in terms of iron oxide chelating affinity (carboxylic *versus* phosphonic acids), hydrophobicity (with or without alkyl fragment), and compared to PEG-devoid polyelectrolyte.

Nuclear magnetic resonance and transmission electron microscopy measurements have originally been combined with fluorescence ones to investigate the impact of the polymer coating on the relaxivity properties of the nanoassemblies and gain insight into the structure of their interface with solutions. To point out the effect of such microstructures on cell interactions, biological studies, facilitated by the high brightness of the fluorescent nanoassembly platform, were performed on malignant pleural mesothelioma (MPM) cancer cells, a very severe cancer contracted after exposure to asbestos and facing poor prognosis of a 12-month median survival time only with the currently administrated drugs. Fluorescence confocal imaging and MRI investigations allowed us to track cell uptake of the magneto-fluorescent NAs by two MPM cell lines and revealed high colloidal and chemical stability, no cytotoxicity effect and progressive

internalization over 24 h, the speed of which depends on the polymer nature. These biological experiments were successfully extended to multicellular tumor cell spheroids (MTCS), known as dense structures of thousands of self-assembled cancer cells and representing novel responsible alternative models of solid tumors inoculated in small living animals. All the reported studies point out the high benefit of using well-controlled polymer coatings such as those issued from controlled radical polymerization, and provide a very general and simple synthetic approach towards efficient and versatile multimodal nanolabels for future *in vivo* cell tracking.

RESULTS AND DISCUSSION

Fabrication of high-density magneto-fluorescent nanoassemblies

The fabrication of magneto-fluorescent nanoassemblies (NAs) proceeded in two stages that allowed us to tailor the stabilizing polyelectrolyte without changing the nature and ratio of the functional constituents of the magneto-fluorescent platform (Figure 1A). In the first step, SPIONs, fabricated following alkaline coprecipitation of iron(II) and iron(III) salts and further oxidation of Fe_3O_4 magnetite into γ-Fe_2O_3 maghemite with iron(III) nitrate, were dispersed in nitric acid solutions (pH = 1.4) at a 0.006 wt. % iron concentration.[31] Adding a concentrated solution of small hydrophobic fluorophores, substituted with phosphonic acid functionality and endowed with solid-state emission properties, simply formed fluorescent organic nanoparticles (FONs) upon nanoprecipitation. FONs usually form by adding a water-miscible solution of fluorophores into a large volume of water. Using water-insoluble fluorophores actually represents a novel strategy to generate FONs that represent an emerging class of emissive nanomaterials for sensitive bio-imaging and have proved to induce no cell mortality and low photobleaching.[32-33] Intermolecular $\pi-\pi$ aggregation, promoted by hydrophobic effects, causes

spontaneous nanoprecipitation of small hydrophobic fluorophores into bright nanoparticles containing more than 10^5 dyes. In our case, the presence of phosphonic units drives self-assembling of SPIONs all around the FON surface through chelation by the outer red-emitting fluorophores placed at the water-FON interface.

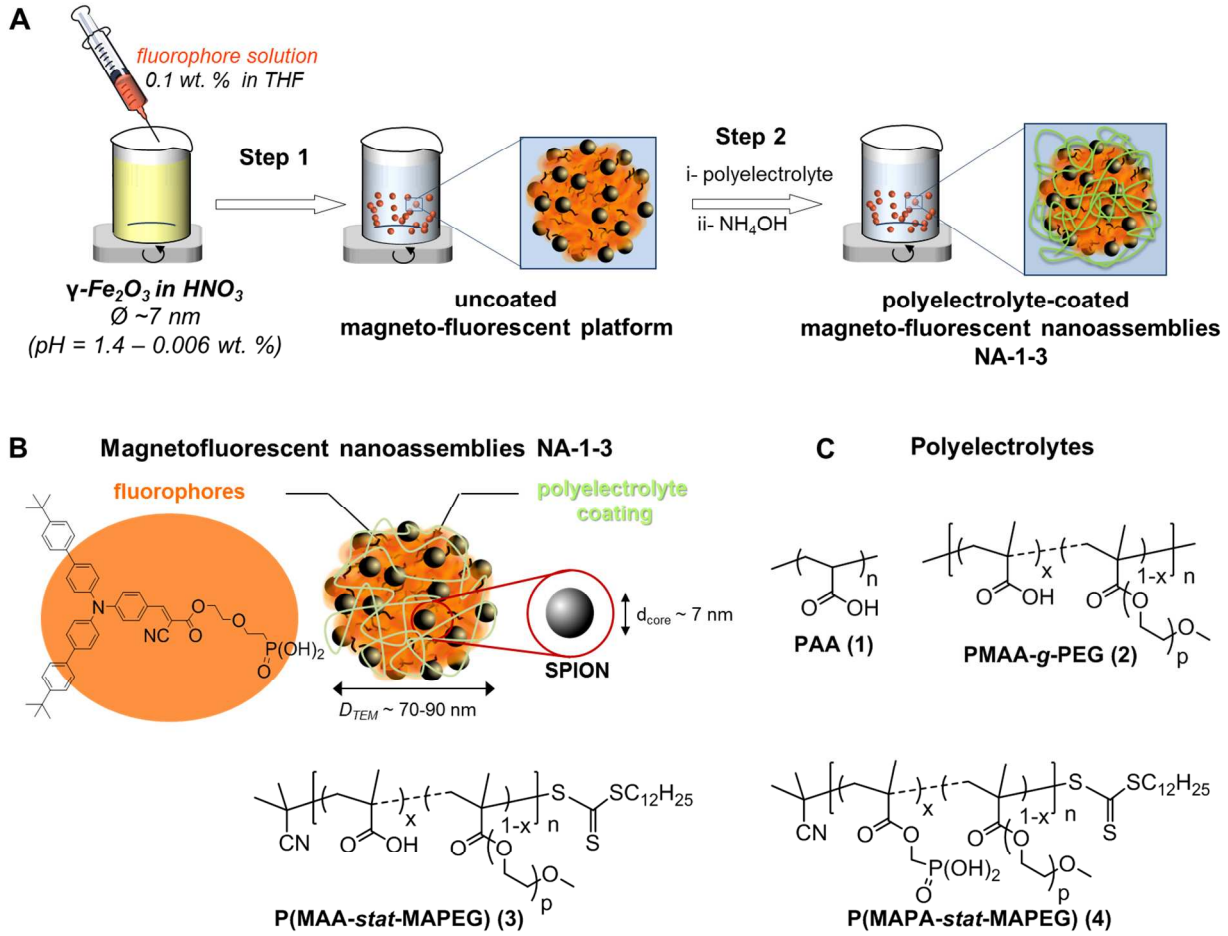


Figure 1. A) Two-step fabrication process of NAs. B) Schematic structure of the magneto-fluorescent NAs stabilized with an anionic polyelectrolyte coating, chelating the shell of magnetic nanoparticles. C) Structure of the synthesized iron oxide-complexing polyelectrolytes.

FON nanoprecipitation actually operates first since SPION complexation requires prior exchange of the labile stabilizing nitrate anions with the strongly interacting phosphonic units.[17]

In this way, SPION incorporation inside the organic core does not occur, and raspberry-like hybrid nanostructures are exclusively obtained with SPIONs attached around the FON surface.

The second step of the fabrication process consisted in the colloidal stabilization of the nanoassembly magnetic shells using polyelectrolytes with strong affinity for iron oxide (Figure 1B). Typical procedure consisting in adding the polyelectrolytes as powders to the acidic solutions of nanoassemblies, increasing pH to 9 by adding a few drops of 1.3 $mol.L^{-1}$ ammonium hydroxide solution to favor deprotonation of the acidic units. After standing for 15 min, the solution was dialyzed using membranes with adapted molecular weight cut-off to remove the non-grafted polymers. To realize such stabilization, various polyelectrolytes with similar sized main functional chains were targeted and differ in their geometry, charge density and hydrophobicity. Commercial linear block PAA_{2000}-*co*-PEG_{2400} copolymers were first used but revealed unable to generate stable nanoassemblies and only intractable material was obtained. This effect tends to recall previous studies on 400 nm-large alumina oxide nanoparticles[34] showing preferential adsorption of block pegylated anionic copolymers involving acrylamido-2-methylpropanesulfonic acid sodium salt monomers (AMPS-b-PEG) over comb-like statistical copolymers (AMPS-stat-PEG). In such block copolymers, the strongly adsorbed sulfonate chains on the nanoparticle surface led to large aggregates that are however stabilized by electrostatic repulsions thanks to the long anionic chains (100 units). We suspect here the same phenomenon, except that the much shorter methacrylate chains (28 units) do not provide enough charge density to stabilize the nanoassemblies while the PEG chain organization may be partly impaired, causing inhomogeneous distributions of steric repulsions. We thus privileged comb-like structures involving poly(methacrylic acid) (PMAA) or poly((methacryloyloxy)-methylphosphonic acid) (PMAPA) as the main chains, and PEG_{2000} or PEG_{1100} as the side-chains

to allow for a better "crown"-like organization of the polymer, with the (meth)acrylate heads pointing to the NA and the PEG side-chains extending in water all way around the NA surface. Short main chains of 25 repetitive units were deliberately targeted since longer chains were reported to bridge several NAs, causing severe aggregation in water.[18] Hence, four polymers were used to assess the effects exerted by a controlled polymer topology and composition as well as the presence of PEG chains on the nanoassembly structures and their interactions with biological media: commercially available PAA with no PEG units (**1**), PMAA-*g*-PEG (**2**) issued from random esterification of PMAA chains with poly(ethylene glycol), P(MAA-*stat*-MAPEG) (**3**), and P(MAPA-*stat*-MAPEG) (**4**) fabricated following reversible addition-fragmentation chain transfer (RAFT) polymerization of PEG-vinyl macromonomers with the corresponding methacrylic acid or (methacryloyloxy)methylphosphonic acid monomers, respectively (Figure 1C). Among the various controlled radical polymerization strategies, RAFT polymerization is nowadays highly favored since it generates water-soluble and biocompatible polymers with narrow polydispersity index and finely controlled architectures.[35-36] In addition, it revealed to be compatible with a large number of functional monomers, and provides easy access to complex copolymers and ready-to-use terminal reactive groups with no need of protection-deprotection steps. In this way, polymers containing various chelating units like carboxylate, phosphonate or sulfur could be easily generated to ensure colloidal stability of metal oxide and metallic nanoparticles upon efficient complexation.[24,37]

The polymer characteristics are gathered in Table 1. The RAFT polymers described in this contribution bear a trithiocarbonate chain-end. It was previously described that this functional group does not induce any noticeable cytotoxicity.[38] The 2-cyano-2-propyl dodecyl trithiocarbonate (CPDTC) functional unit was thus used as a RAFT agent suitable for the

controlled polymerization of methacrylates. Its alkyl substituent advantageously imparts the polymer architecture with additional hydrophobicity, which allowed us to study the direct impact of a partly hydrophobic coating on MRI performance and cellular uptake without modifying the overall number anionic units and their complexing ability.

Table 1. Structural characteristics of iron oxide-chelating polyelectrolytes employed as coatings.

Polyelectrolyte	M_n (g.mol^{-1})	M_w (g.mol^{-1})	PI[a]	n[b]	p[b]	x (%)[b]
1	n.a.	1.8×10^3	n.a.	24	0	100
2	5.86×10^4	10.9×10^4	1.87	30	43	78
3	3.99×10^4	5.19×10^4	1.30	30	43	80
4	2.68×10^4	3.75×10^4	1.40	25	23	60

[a] PI designates the polydispersity index determined from size exclusion chromatography analyses using DMF as a solvent. [b] n: degree of polymerization of the main chain; p: degree of polymerization of the side chains; x: molar fraction of the acid comonomer units in the main chain respectively, as depicted in Figure 1C.

The tolerance of the RAFT mechanism to various functional groups enabled the direct copolymerization of a PEG methacrylate macromonomer with either MAA or MAPA, following simple synthetic procedures in solution. The comb-like topology was obtained here by a graft-through method.[39] The statistical distribution of the two types of monomer units was ensured by the similar reactivity ratios of the selected methacrylate comonomers.

Influence of the PEG coating and complexing units on the nanoassembly structure

Transmission electron microscopy (TEM) measurements revealed a tremendous difference in the nanoassembly structure depending on the complexing units of the polyelectrolytes. Phosphonic acid-containing polyelectrolytes yielded neat separation between maghemite nanoparticles and

clearer globules, ascribed to organic matter due to their lower electronic contrast (Figure S1). By contrast, all polyelectrolytes containing carboxylic acid units generated well-defined spherical structures (here dubbed **NA-1**, **NA-2** and **NA-3**), as showed by TEM imaging (Figures 2A). Here, we want to point out that no such nanoassemblies could be formed by simply mixing polymer solutions with SPIONs (Figure S2).

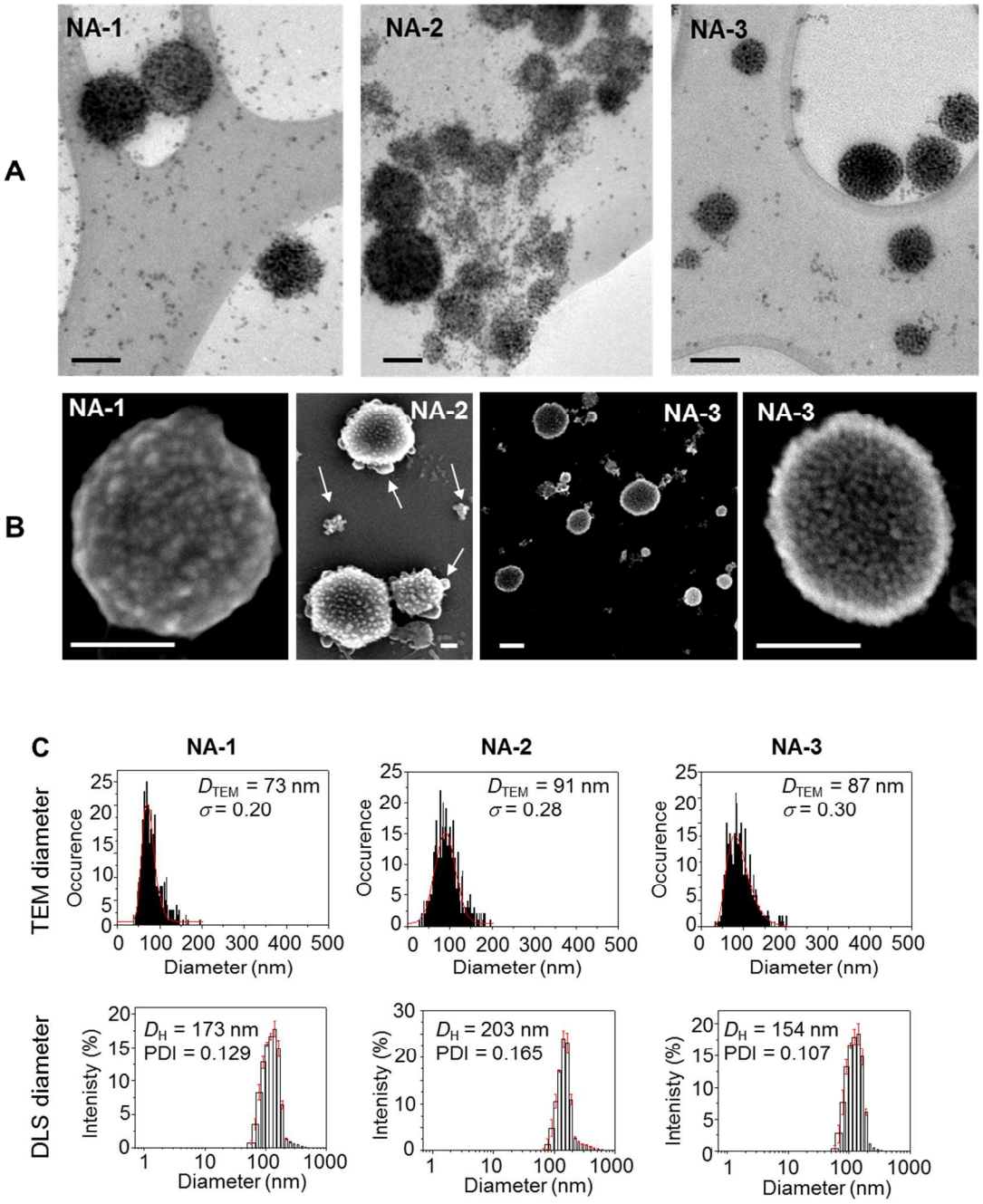


Figure 2. A) TEM imaging on holey carbon-coated copper grids, and B) SEM imaging on silicon wafer of magneto-fluorescent nanoassemblies **NA-1**, **NA-2** and **NA-3**. Scale bar: 100 nm. White arrows indicate fused or melt nanoassemblies **NA-2**. C) Histograms of diameter distributions of **NA-1**, **NA-2** and **NA-3** assessed by TEM measurements (D_{TEM}) and DLS analyses in water (D_H). Note that the TEM diameter distributions follow a lognormal function (red curve).

Since TEM imaging of the acidic nanoassembly solution, namely before adding any polyelectrolyte, showed also the same raspberry-like structure,[17] we concluded that poly(phosphonic acid) is so complexing with respect to the fluorescent core that it stripped SPIONs out and pulled them apart. No improvement could be obtained by decreasing the molar fraction of phosphonic acid monomer units down to 20 % to avoid such competitive complexation interactions as detected by TEM imaging (Figure S3). Obviously, choosing the right order in the complexation affinity from the center to the outer part of multi-shell structures reveals to be crucial to achieve stable NAs and tremendous solubilization of a metal oxide core upon privileged cation complexation by the shell was even reported in the past.[40] A similar situation was already observed when the fluorophores of the core were substituted with a carboxylic acid unit.[18] The latter proved insufficient to retain the complexed iron oxide nanoparticles after coating with poly(acrylic acid) exerting competitive multifold attachment. Hence, only PAA (**1**) and PMAA-based polyelectrolytes (**2**) and (**3**) were retained for the following studies.

When looking carefully at the corresponding NA structure as a function of the polyelectrolyte structure, a superior density of SPIONs could be observed at the surface of both **NA-2** and **NA-3**. For the latter two, less isolated maghemite nanoparticles could be observed contrary to **NA-1**

involving a PAA stabilizing coating (Figure 2A). Interestingly, scanning electron microscopy (SEM) imaging reveals nanoassemblies twice as large as those detected by TEM, along with giant well-defined aggregates (400-500 nm-large) (Figure 2B). Since argon plasma treatment for a few seconds was applied to gain electronic contrast, we suspect partial melting of the self-assembled organic core of the nanossemblies and even fusion for several of them. This results in enlarged diameters as well as large aggregates with small peripheral protuberances (especially for **NA-2**) ascribed to the initial nanoassemblies. Thus, SEM imaging indirectly indicated the soft core's character of the raspberry-like magneto-fluorescent nanoassemblies. Overall, the mean dry diameters D_{TEM} evaluated by TEM size lognormal distribution varied between 70 and 90 nm with a relatively low standard deviation ($\sigma < 0.30$) (Table 2-Figure 2C). The pegylated NAs were found slightly larger by a few nm as a result of the larger size of polymers (**2**) and **(3)**. Interestingly, the hydrodynamic diameters D_H of NA dispersions in water, measured by dynamic light scattering (DLS), followed quite a distinct trend. The D_H values were found at 170-200 nm, systematically larger than the dry diameter D_{TEM} ones, as a result of the surrounding hydration shells. The nanoassemblies **NA-3** appeared smaller with D_H = 154 nm, which suggests a less extended coating in water due to the presence of the hydrophobic [41] chains of the RAFT agent, as already reported for PEG chains grafted to phospholipids with long alkyl chains.[42] The lack of similar trends between both D_H and D_{TEM} values emphasizes the importance of complementary measurements and the complex impact of coulombic and dipolar interactions on the recruitment of water molecules, as also exemplified by the charge potential ζ measurements. A lesser zeta potential ζ was found for **NA-2** with PMAA-*g*-PEG coating, issued from conventional polymerization whereas **NA-1** and **NA-3** with PAA and RAFT-based coatings respectively, yielded largely negative ζ values ($\zeta < -51$ mV). All nanoassemblies show similar hydrodynamic

diameters in water, NaCl solutions of varying concentration (0.1, 0.3 and 0.5 mmol.L^{-1}), HBSS and RPMI, indicating no aggregation process (Figure S4A). A 15-day follow-up of the nanoassemblies in potential storage media (water, NaCl, HBSS) revealed also large colloidal stability since no aggregation could be detected (Figure S4B). Far from being contradictory, the large absolute ζ value and the low D_H value for **NA-3** indicate the formation of a very compact shell of PEG chains at the nanoassembly surface, leaving few access to water molecules, which can exert quite an influence on the MRI contrast and relaxivity properties.

Table 2. Structural and photophysical characterizations of magneto-fluorescent NAs coated with PAA (**1**), PMAA-*g*-PEG (**2**) and P(MAA-*stat*-MAPEG) (**3)** polyelectrolytes.

NA	D_{TEM} (nm) (Std Deviation)	D_H (nm) / PDI	ζ (mV)	[Fe] (mM)	λ^{max}(abs) (nm)	λ^{max}(em) (nm)	Φ_f ($\times 10^{-2}$)
NA-1	73 (0.20)	173 / 0.129	-51.9 ± 6.4	0.384	423	614	1.45
NA-2	91 (0.28)	203 / 0.165	-32.6 ± 5.7	0.543	428	612	0.83
NA-3	87 (0.30)	154 / 0.107	-53.0 ± 10.5	0.459	429	595	0.20

Photophysical properties and impact of the polymer coating on emission properties

The absorption spectra of NAs appear very similar and the contributions of the three structural components could be noticed (Figure 3): i-the low-energy band at 420 nm is ascribed to a charge transfer transition within the FONs' fluorophores; ii-the monotonous increase in absorbance at higher energy relies on the γ-Fe_2O_3 nanoparticle extinction spectrum; iii- finally, the large tail around 200-250 nm is related to the UV absorption of the C=O chromophores contained in the PAA or PMMA carboxylate units (Figure S5). For P(MAA-*stat*-MAPEG) coating, one could

distinguish an additional maximum at 311 nm that is characteristic of the RAFT trithiocarbonate ends, remaining uncleaved after treatment with ammonia.[43] Excitation in the absorption band of the fluorophores at 450 nm provided an emission signal whose maximum varies between 595 and 614 nm (Figure 3, Table 2). This emission band is typical of the FON core one which is centered at 605 nm in water in the absence of SPIONs.[44] The large Stokes shift, defined as the difference in energy between the absorption and emission maxima of the nanoassembly spectra, were found around 7000 cm^{-1}. This large energy difference is worth noting since it greatly facilitates label detection in live cells where endogenous fluorophores usually display autofluorescence, weakly shifted from excitation.

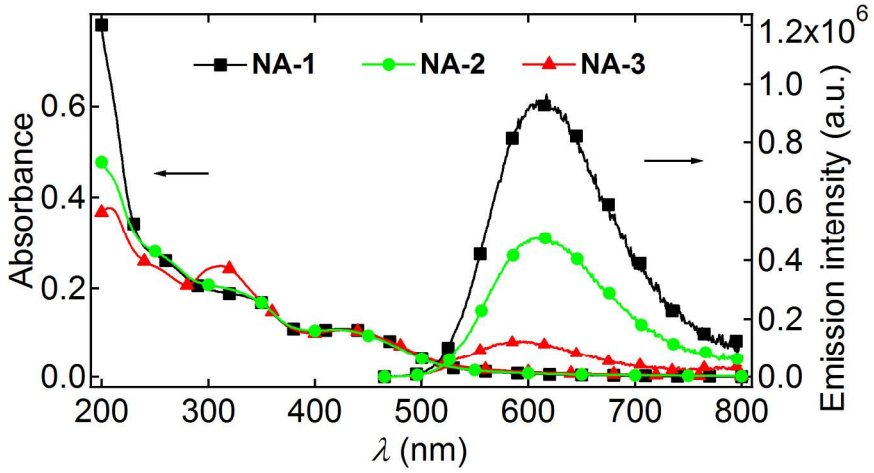


Figure 3. UV-vis absorption (left axis) and emission (right axis, λ_{exc} = 450 nm) of aqueous solutions of magneto-fluorescent nanoassemblies **NA-1**, **NA-2** and **NA-3**.

Since the FON fluorophores display strong positive solvatochromism,[45-46] the hypsochromic shift observed for **NA-3** compared to **NA-1** and **NA-2** again reflects significant differences in the interactions with water molecules, which may stem from the lipophilic chains of the RAFT-ends organized in a close and tight fashion at the surface of the magneto-

fluorescent structures. Such assumption is reinforced by the notable decrease in fluorescence emission quantum yield observed with **NA-3** compared to the other two NAs. Recent studies have actually reported on the efficient dynamic and static emission quenching of fluorophores in the presence of RAFT polymers containing dithiocarbonate transfer agents,[47] which implies close vicinity between RAFT polymers and fluorophores. Such dynamic quenching was also confirmed by fluorescence time-resolved measurements recorded at 600 nm after a 450 nm excitation (Table S1-Figure S6). A four exponential fit was required to model the fluorescence decay. While the major three lifetime components τ_2, τ_3 and τ_4 were found almost identical for all nanoassemblies at 0.52-0.57, 0.14-0.16 and 0.02-0.03 ns respectively, the longer component τ_1 largely differs between **NA-3** at 1.07 ns, and **NA-1** and **NA-2** at around 2 ns. From the intensity-averaged fractions, the latter time component contributes to the total emission decay by only 1.5-5 %. We thus presume that τ_1 characterizes the fluorophores that are placed at the periphery of the nanoplatform and sense in a more privileged way the polyelectrolyte coating. The quenching phenomenon observed for **NA-3** thus indirectly proves the strong attachment of RAFT-derived P(MAA-*stat*-MAPEG) at the surface of the magneto-fluorescent nanoassemblies since dynamic quenching is very negligible at concentrations as low as 10^{-4} mol.L^{-1} for both the polyelectrolyte and fluorescent units.

All the above-reported structural and photophysical characterizations conduct us to propose a tentative scheme to describe the organization and extension of the polyelectrolyte chains around the FON surface, which would lead for polyelectrolyte (**3**) to stronger interchain interactions with γ-Fe_2O_3 nanoparticles due to the less extended chains, especially in water (Figure S7).

ZFC-FC magnetic measurements and low-temperature hysteresis

In order to probe the possible influence of the polyelectrolyte coating onto the magnetic properties of the nanoassemblies, we performed static magnetic measurements. Zero-field-cooled (ZFC) and field-cooled (FC) curves, giving information on magnetic interactions between SPIONs at the FON surface, were traced by recording the temperature dependence of the magnetization under a 50 Oe magnetic field (Figure 4A).

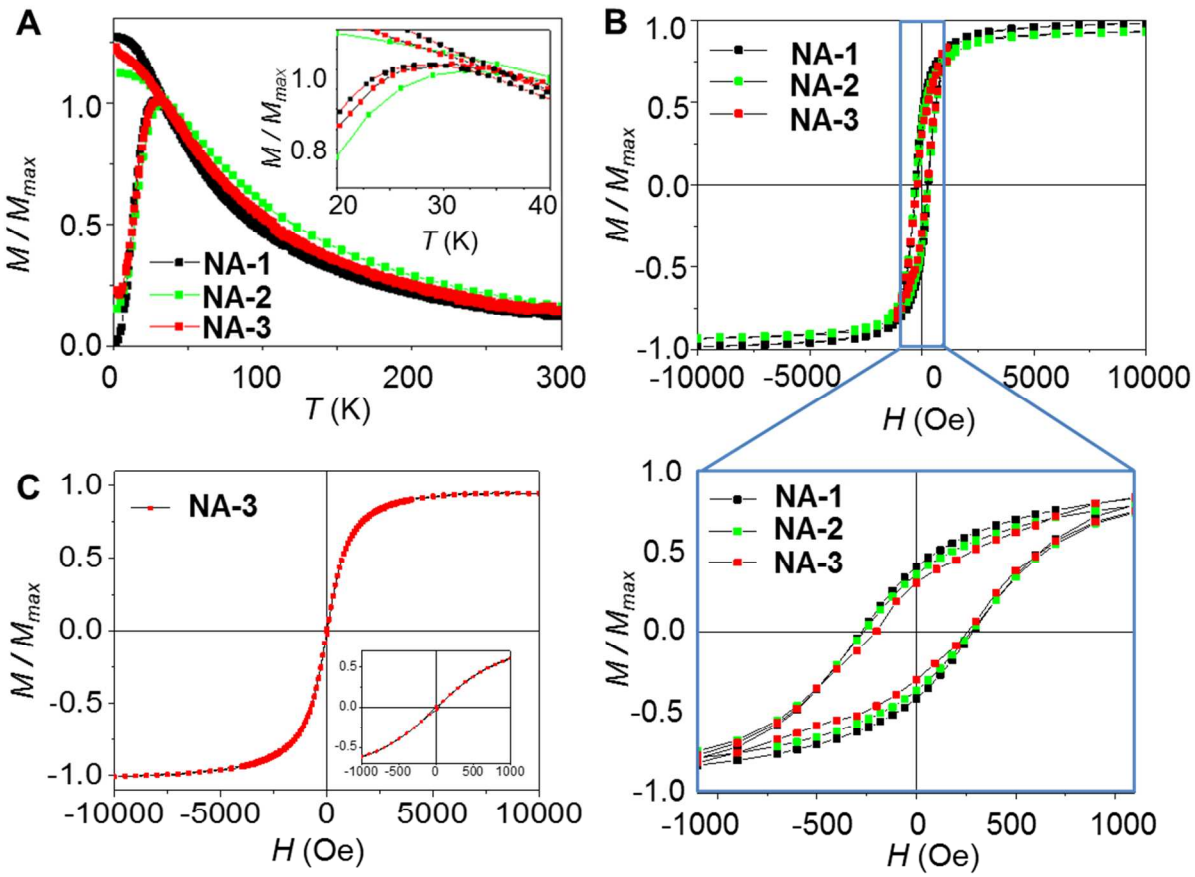


Figure 4. A) ZFC-FC curves for magneto-fluorescent nanoassemblies **NA-1**, **NA-2** and **NA-3**; the curves are normalized to the maximum of the ZFC magnetizations. B) Plot of magnetization M/M_{max} versus applied magnetic field at 2.5 K and enlargement at low magnetic fields. C) Plot of magnetization M/M_{max} versus applied magnetic field at 310 K for nanoassemblies **NA-3**.

For all samples, the thermal irreversibility characteristic of an assembly of single domain magnetic particles is observed below ca. 40 K, pointing out that the investigated systems are in the superparamagnetic state at room temperature. Except for a slight shift of the maximal temperature T_{max} at 35 and 33 K for **NA-2** and **NA-3** respectively, against 28 K for **NA-1** signing larger dipole-dipole interactions and more closely arranged SPIONs upon coating with pegylated polyelectrolytes (Table 3), all curves display the same shape in agreement with the same general NA architecture and identical sized SPIONs (Figure 4A). We thus recorded the magnetization evolution as a function of the magnetic field at 2.5 K where ZFC-FC measurements indicate that SPIONs are blocked in their ferromagnetic state (Figure 4B). Again, the magnetization curves superimposed fairly well with the values of the reduced remanence M_R/M_S (namely, the ratio of the remanence to saturation magnetization) in the 0.32-0.40 range, which as commonly observed for maghemite nanoparticles.[15] Similarly, the coercive field H_c for all samples also changed only slightly from 18 to 22 $kA.m^{-1}$ (226 to 276 Oe) when varying the nature of the polyelectrolyte coating. Conversely, at room temperature, namely 310 K, no irreversibility was observed, indicating that all nanoassemblies are in the superparamagnetic state (Figure 4C and Figure S8).

From these measurements, we can thus conclude that the static magnetic properties of all NAs are exclusively ruled by the shell of SPIONs attached on the FON core, and are almost independent of the nature of the polyelectrolyte coating.

NMRD measurements and MRI contrast as a function of the polyelectrolyte coating

As MRI contrast brought by SPIONs is dictated by their relaxivity properties, we recorded their NMRD profiles which give access to the longitudinal r_1 and transverse r_2 relaxivities. Since relaxation of water protons close to the NA surface is also probed, any microscopic difference due to the polyelectrolyte coating can be inferred (Figure 5). The difference between the data

recorded at room and physiological temperatures being within 10 %, we reported the NMR results obtained at room temperature to better discuss the physical mechanisms involved in the nuclear relaxation. For comparison purposes with a clinically used contrast agent, we retained Endorem® made of a multicore structure (D_H ~ 120 nm) of 5 nm-large SPIONs self-assembled with dextran polymer.

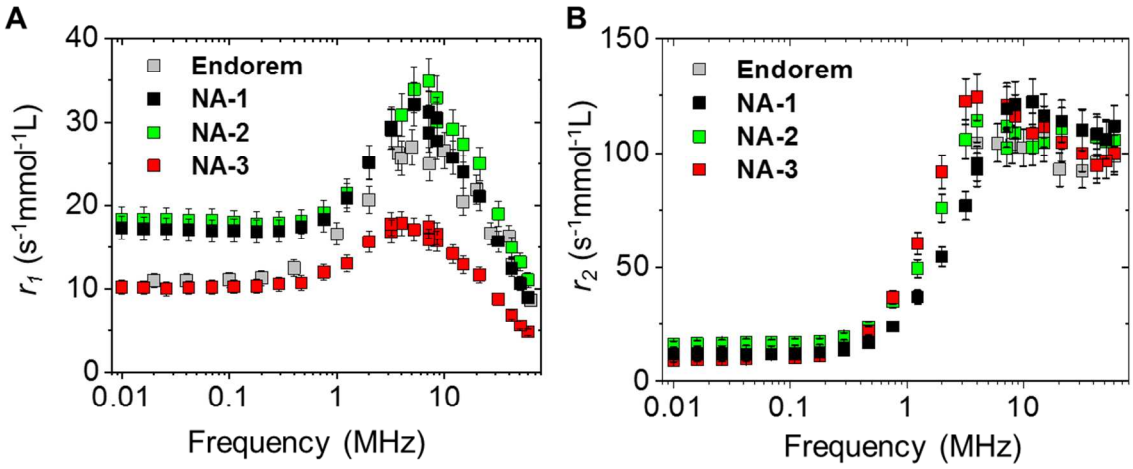


Figure 5. A) Longitudinal r_1, and B) transverse r_2 relaxivities of nanoassemblies **NA-1**, **NA-2**, **NA-3** and commercial contrast agent Endorem® as a function of proton Larmor frequency.

As SPIONs induce strong distortions of the local magnetic field, proton relaxation is largely dominated by a spin-spin relaxation mechanism, giving rise to r_2 relaxivities by far larger than r_1 ones for frequencies higher than several MHz. Hence, most of the studies have focused on measuring r_2 values just at the (very few) clinical fields,[12-13,48-49] but do not report on r_1 *vs* frequency behavior. And yet, the later investigations provide precious information on the dominant mechanisms of nuclear relaxation in different frequency ranges and on the water diffusion time. Therefore, they give insight into the nanoassembly structure, its spin dynamics and the hydrated environment. The r_1 vs frequency (ν) profiles for all three NAs display a typical superparamagnetic behavior: a decrease in relaxivity at high frequency, a mid-field peak at ν_{max},

and a low field plateau (Figure 5A).[50] Interestingly, the typical "dispersion" feature for SPIONs with diameter less than 10 nm, occurring between the frequency corresponding to the maximum r_1 and the low frequency region, does not appear clearly in the $r_1(\nu)$ curves. Since the dispersion, generally reduced for small particles, is correlated to the magnetic anisotropy of the SPIONs, we can conclude in the case of NAs on an increase in anisotropy.[51] At high frequencies, Curie relaxation prevails due to the presence of a high local magnetic field induced by the magnetization of SPIONs, subjected to a relatively high external static magnetic field, this local field being dynamically mediated by the diffusion correlation time. The curves for all NAs converge toward similar values as expected for the studied samples, displaying identical static magnetic behaviors. The most striking features are the significantly lower r_1 values found for **NA-3** at ν_{max} and in the low frequency region (Table 3).

Table 3. Maximum longitudinal r_1 and transverse r_2 relaxivities [@corresponding frequency], and r_2/r_1 *ratio* measured at 25 °C for nanoassemblies **NA-1**, **NA-2** and **NA-3**, and commercial contrast agent Endorem® for comparison, and magnetic properties of nanoassemblies **NA-1**, **NA-2** and **NA-3** measured at 2.5 K.

	r_{1max} ($s^{-1}mmol^{-1}L$) [@ν(MHz)]	r_{2max} ($s^{-1}mmol^{-1}L$) [@ν(MHz)]	r_2/r_1 @8.5 / 21.3 / 60 MHz	T_{max} (K)	H_c (kAm^{-1})	M_r/M_s
NA-1	32 [6]	122 [12]	4 / 5 / 12	28	22	0.40
NA-2	34 [7]	115 [4]	3 / 4 / 9	35	22	0.35
NA-3	19 [5]	125 [4]	7 / 9 / 21	33	18	0.32
Endorem®	28 [7]	105 [4]	4 / 5 / 11	-	-	-

Since all NAs share the same core-shell configuration and static magnetic properties, the difference encountered in the r_1 relaxivity of **NA-3** cannot be related to the latter effects. We

suggest a possible explanation that could rely on the dynamics of water molecules, namely their diffusion, retention time as well as their access closer or farther from to the magnetic shell.[42,52] The smaller hydration sphere found for **NA-3** by DLS (see Table 2) suggests the existence of a restricted solvation sphere due to strongly attached PEG side-chains and hydrophobic dodecyl RAFT-end chains. At a first glance, the restricted solvation sphere could erroneously evoke a closer diffusion of water to the NA surface. Actually, the presence of a hydrophobic part in the **NA-3** polyelectrolyte prevents water to diffuse into the coating, while the hydrophilicity of the other nano-assemblies allows water molecules to move closer to the SPIONs core inside the NA coating itself. Therefore the difference in r_1 relaxivity could be explained by the presence of dodecyl RAFT-end chains in **NA-3**.

Contrarily to r_1 dispersions, similar r_2 profiles were found for all NAs with maximum r_2 values of around 120 $s^{-1}mmol^{-1}L$ in agreement with identical magnetic cores (Figure 5B). In fact, local dephasing of the nuclear magnetization is mostly caused by the high electronic magnetization of the SPIONs clustered around the FON core. This represents the prevailing mechanism inducing nuclear transverse relaxation, which is partially described by an approximate heuristic model in the framework of the so called Motional Average Regime (MAR).[10,53] Unfortunately, the actual models (like the universal scaling law proposed by Sandre et al.)[54] are not able to describe the whole transverse NMRD curve (r_2 vs. ν) or explain the relaxation mechanisms as a function of the applied magnetic field. Nevertheless, since the transverse relaxivity r_2 represents the fundamental parameter to assess the MRI efficiency for a superparamagnetic material, the reported experimental data demonstrate that our nanoparticles act as promising negative contrast agents. Moreover, the low r_1 and high r_2 values for **NA-3** yields a large r_2/r_1 ratio that represents a parameter as important as r_2 relaxivity to assess the efficiency of negative contrast agents. In the case of NA-3, such ratio is about 21 at 60 MHz

clinical frequency, which is two to threefold higher than those for **NA-1**, **NA-2** and Endorem®. These NMRD studies demonstrate the large importance of considering both the transverse and longitudinal relaxivities to probe the interface of complex magnetic nanostructures and evaluate the microscopic mechanisms underlying the nuclear relaxation that is quite largely influenced by the spin topology and water diffusion path. Deciphering the fundamental physical mechanisms ruling the nuclear relaxation should thus open novel perspectives regarding the synthesis of novel coatings with high efficiency (namely, higher transverse and/or longitudinal relaxivities) for improved MRI contrast.

Kinetics of cellular internalization and cell toxicity assays in mesothelioma cancer cells

Adherent mesothelioma cells (Meso 11), a cell line established from pleural fluid of patients affected by MPM, were incubated with **NA-1**, **NA-2** and **NA-3** in RPMI medium supplemented with 10 % serum. The amount of administrated nanoassemblies was referred to their iron content, titrated by elemental analyses by means of inductively coupled plasma optical emission spectrometry (ICP-OES) following acidic mineralization. Kinetics of NAs' uptake was carried out by following the fluorescence and magnetic responses of single cells. The fluorescent signal and cell viability were assessed by means of imaging flow cytometry after usual protocols to detach the cells, and treatment for 30 min with Zombie NIR®, serving as a fluorescent marker that lights up in the presence of dead cells. In this way, a single excitation at 488 nm allowed for dual excitation of the nanoassemblies and fluorescent marker, and simultaneous detection of their respective emission signals in two distinct non-overlapping channels (channel 3: 560-595 nm for NAs; channel 12: 745-800 nm for Zombie NIR® permeant to dead cells). Figure 6A displays the kinetics of uptake over a 24 h incubation period for **NA-1**, **NA-2** and **NA-3**, at an

iron concentration of 2-3 µmol.L^{-1}. The mean fluorescence intensity (MFI) steadily increased for all three nanoassemblies and started saturating after around 16 h for **NA-1** and **NA-2**.

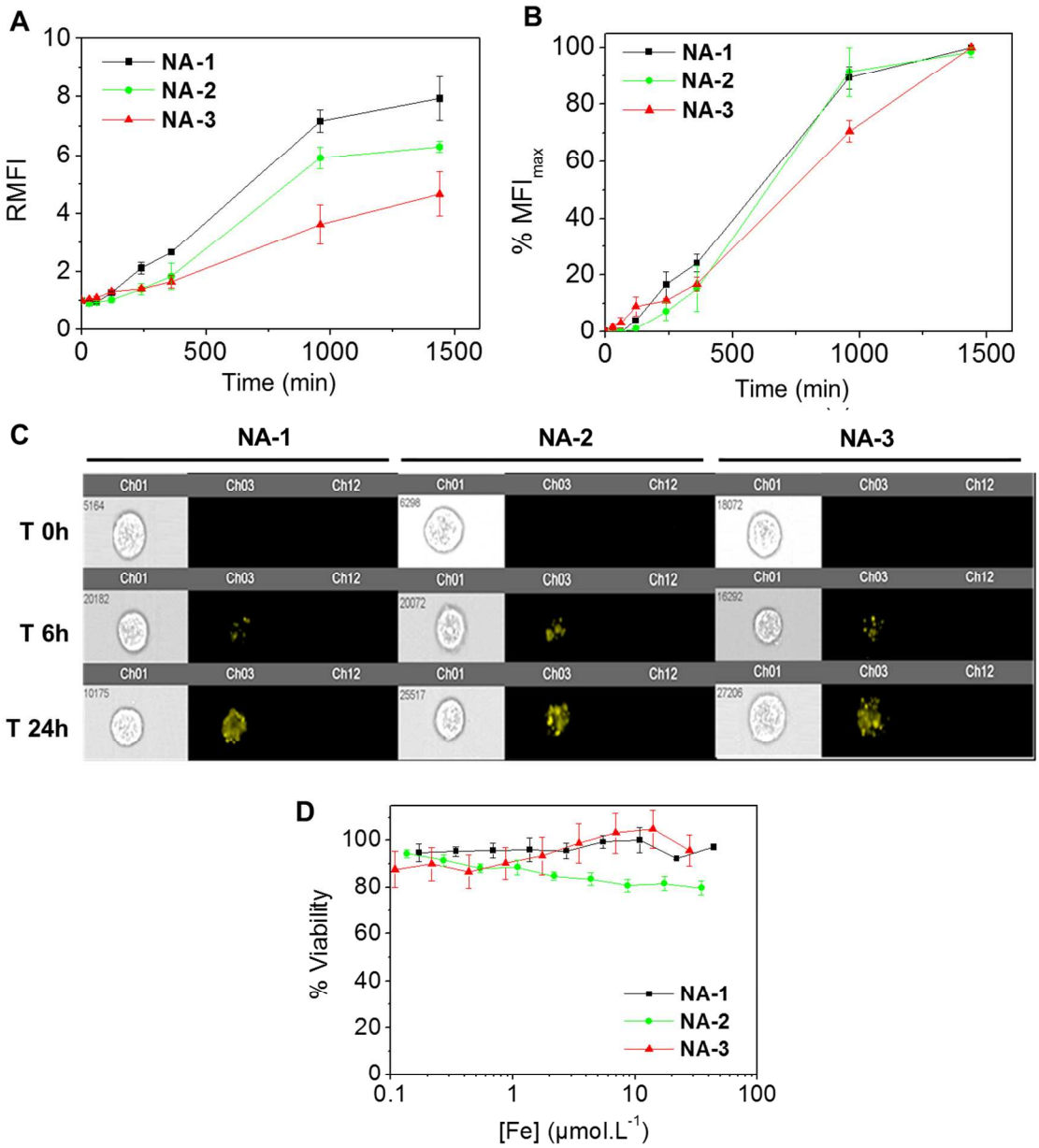


Figure 6. Meso 11 cells incubated with nanoassemblies **NA-1**, **NA-2** and **NA-3** in RPMI supplemented with 10 % FBS serum. A) Absolute, and B) normalized mean fluorescence intensity (MFI) evolution over time of incubation. C) Imaging flow cytometry at 0 h, 6 h and 24 h. D) Cell viability assay after a 72 h incubation period for [Fe] = 0.1-100 µmol.L^{-1}.

At very early times up to 4 h, only a few nanoassemblies were internalized. This result was confirmed by imaging flow cytometry showing dimmed fluorescence signals at 6 h and very bright ones at 24 h inside the cells (Figure 6C). The slow rate of uptake is actually related to the negative charge of the investigated nanoassemblies that have to overcome the electrostatic repulsions exerted by the phospholipids of the cytoplasmic membrane.[55] Interestingly, at longer times, **NA-3** tend to internalize at a significantly slower rate compared to **NA-1** and **NA-2**, as exemplified by the normalized MFI signal (Figure 6B). This result is quite surprising since both PMAA-*g*-PEG and P(MAA-*stat*-MAPEG) contain the same functional groups and PEG chain length. At first, one could think at differential interactions with the serum proteins that adsorb on the nanoparticle surface and govern the dynamic of uptake.

We thus investigated by electrophoresis the nature of the protein corona that could form around all three kinds of nanoassemblies. The latter were incubated for 1 h at an iron concentration of [Fe] = 2.1 – 2.9 mmol.L^{-1} in cell culture medium (RPMI medium supplemented with 10 % FBS). The nanoparticle-protein complexes were extracted by centrifugation and the supernatant loaded into the wells of a polyacrylamide electrophoresis gel. After migration for 90 min and revelation under UV irradiation, three bands for all NAs were visible (Figure S9). One of them was found in the range of 50-60 kDa molecular weight and could be identified as being bovine serum albumin (BSA), as confirmed by comparative elution of a BSA reference sample. The other two bands were found in the range of 10-30 kDa and attributed to apolipoproteins (apoAI and apoAII) in agreement with common reports in the literature regarding the interactions of iron oxide nanoparticles with human serum proteins.[56-57] It is worth noting that very few non-specific interactions occur between the nanoassemblies and cell culture medium despite the relatively high NA concentration used in the study to distinguish protein complex

traces. This observation features weak protein adsorption, which is highly sought for further *in vivo* investigations. As all three NAs display the same patterns under the investigated experimental conditions, we can reasonably ascribe the distinct uptake rates of **NA-3** nanoassemblies to their intrinsic comb-like polyelectrolyte coating. As deduced from the above photophysical and magnetic studies, the hydrophobic RAFT polymers tend to organize in quite a compact fashion at the nanoassembly surface. The generated nanoarchitectures thus display a distinctly structured surface, which makes the uptake rate continuous with no negative impact on cell viability.

This observation is of utmost importance as the actual tendency is to advertise fast uptake for fast therapeutics delivery with little consideration of cytotoxicity. Indeed, positively charged nano-objects display faster internalization in usually less than 1 h, which causes large cell mortality due to extensive permeation of the cell membrane, unable to readapt in front of the sudden flow of nanoparticles.[58] In our case, cell viability assay based on the use of 3-[4,5-dimethylthiazol-2-yl]-2,5- diphenyltetrazolium bromide compound (MTT reagent) after 72 h of incubation with the different NAs, revealed no cytotoxicity for **NA-3** and **NA-1** over the broad range of iron concentrations from 0.1 to 100 $\mu mol.L^{-1}$ (Figure 6D). A slightly higher level of cytotoxicity for **NA-2** was found although such a value, below 20 %, is often regarded as non-significant. The images collected using imaging flow cytometry show no change in the cell phenotype over 24 h, which reinforces the non-cytotoxic properties of all nanoassemblies (Figure 6C). To ascertain the cellular entry of both the magnetic and fluorescent components of the nanoassemblies, complementary magnetophoresis measurements were performed on cells incubated with Meso 11 after 4 h, 8 h and 24 h ([Fe]=200 $\mu.mol^{-1}$). Such experiments consist in measuring the velocity of cells subjected to a magnetic field gradient, which is directly correlated

with the cellular load of iron oxide. Due to the low amount of magnetic materials used with regard to literature and the associated uncertainty, comparative results between the distinctly coated NAs would be irrelevant. As illustrated in Figure S10, all NAs nicely followed the same trend of continuous iron oxide uptake over 24 h. These results indicate tight association of both the magnetic shell onto the fluorescent core, making such nano-objects particularly attractive for bimodal imaging. They thus emphasize the clear advantage of nanoassemblies comprising FONs as fluorescent cores and a shell of magnetic nanoparticles. In this way, very bright fluorescent and magnetic nanostructures are obtained, enabling high detection sensitivity and easy follow-up.

Multimodal imaging properties in live cells

To prove the potentiality of the magneto-fluorescent NAs as multimodal imaging agents, we performed confocal fluorescence microscopy, MRI and TEM investigations of cells after NA incubation for 24 h. The culture medium was washed with PBS to remove NAs in excess. The cells were treated successively with Alexa Fluor® 647 conjugate of wheat germ agglutinin (WGA) (green) and Hoechst (blue) to stain the cell membranes and nuclei respectively (Figure 7A). Confocal fluorescence imaging revealed very bright dots, depicted in red, which can be assigned to internalized NAs. An XY projection clearly revealed the internalization of NA and their unambiguous location inside the cytoplasm. Again, no impact of the nanoassemblies could be noticed on the adherent Meso 11 cells that keep their elongated shape, which confirms the cell viability assays and absence of cytotoxicity. To gain even better definition of the NA location, we took advantage of the iron oxide electronic contrast and performed TEM experiments. Most of protocols involve cell detachment and centrifugation to generate a cell pellet, which can damage the cell architecture. To avoid partial cell destructuration, cells were directly fixed in

Epon resin and properly stained. TEM observation of the cell monolayers showed well-contrasted dark dots, included in larger structures that remind of endosomes, especially for **NA-1** (Figure 7B).

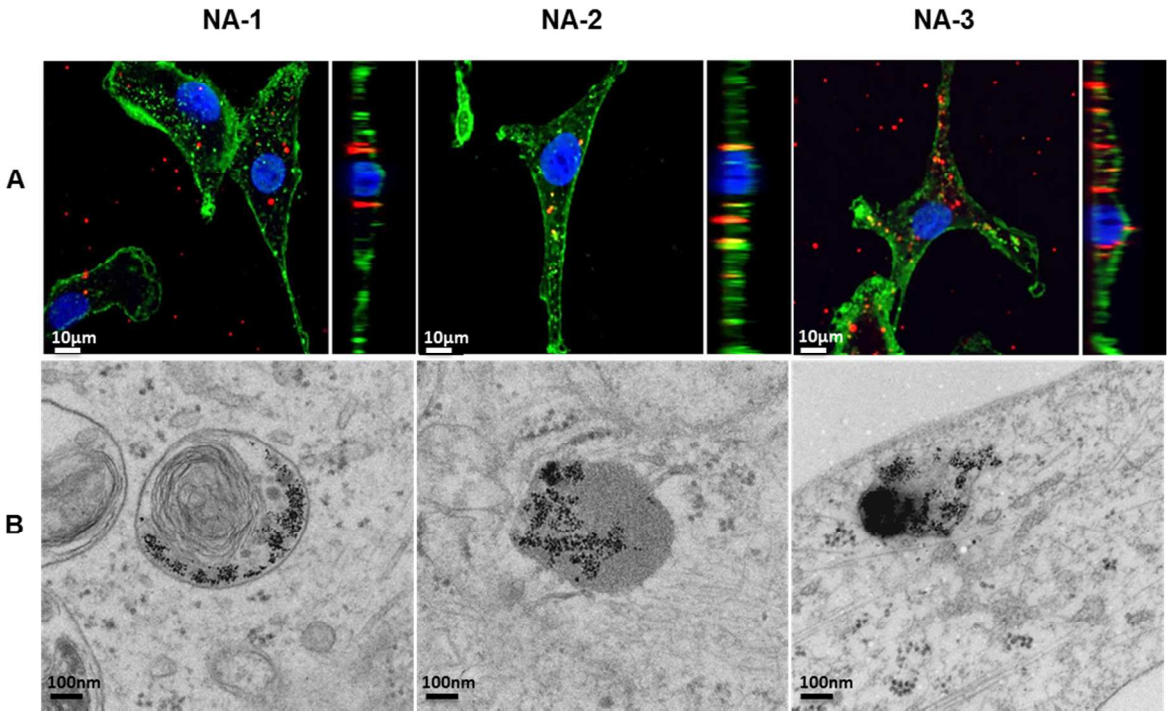


Figure 7. Meso 11 cells incubated with magneto-fluorescent nanoassemblies **NA-1**, **NA-2** and **NA-3** for 24 h. A) Confocal fluorescence microscopy showing the nanoassemblies in red, the WGA-AlexaFluor® 647-stained cellular membrane in green, and the Hoechst-stained nuclei in blue. Pictures include an XY orthogonal projection. B) TEM imaging of fixed cells.

Careful observations at such a magnification let us notice small packets of dark dots instead of a random dispersion. This feature is to correlate with previous *in vivo* and *in vitro* observations where the magneto-fluorescent structure was kept, with no dissembling of the fluorescent core from the magnetic shell.[22] Therefore, incrementing stabilizing PMAA or PAA-based polyelectrolyte coating with PEG chains does not impair the emission properties and the

ability of generating tight hybrid nanoassemblies. The novel pegylated NAs thus represent very attractive agents for correlative light electron microscopy that is currently stirring much attention since high spatial resolution of biological structures can henceforth be achieved.[2]

The NA multimodality property is extended to MRI investigations to anticipate *in vivo* experiments in the future. A novel series of cells incubated with the magneto-fluorescent NAs at an iron concentration of 2-3 $\mu mol.L^{-1}$ for 24 h was prepared. It is worth noting that such a concentration is actually 10 to 10^2 times lower than the commonly recommended iron doses for conventional MRI on humans (0.5-10 $mg.kg^{-1}$).[5960] After the usual recuperation procedure, the cells were deposited in small wells dug into a matrix of well-degassed 1 % low-melting agarose gel, filling a glass cylinder (Figure 8A).[61] The wells were sealed by pouring on top a still-liquid and cooled agarose solution. Careful air degassing is requested to avoid dramatic quenching effects of MRI contrast due to entrapped paramagnetic dioxygen. A T2 sequence was used in relation with the negative contrast properties of iron oxide nanoparticles. Unlike control cells devoid of NAs and providing no significant signal, the cells incubated with all NAs showed a clear MRI dark contrast (Figure 8B). When taking the control cells as a reference, we found an average darkening MRI contrast enhancement (ENH) of -80 %. This value is notably high given the low amount of SPIONs, which validates the strategy of assembling individual superparamagnetic nanoparticles around a larger fluorescent core to generate enhanced responses. The resulting supramolecular architecture, stabilized by additional polyelectrolytes, thus keeps the properties of the isolated units while offering novel ones thanks to the high density of associated functional units.

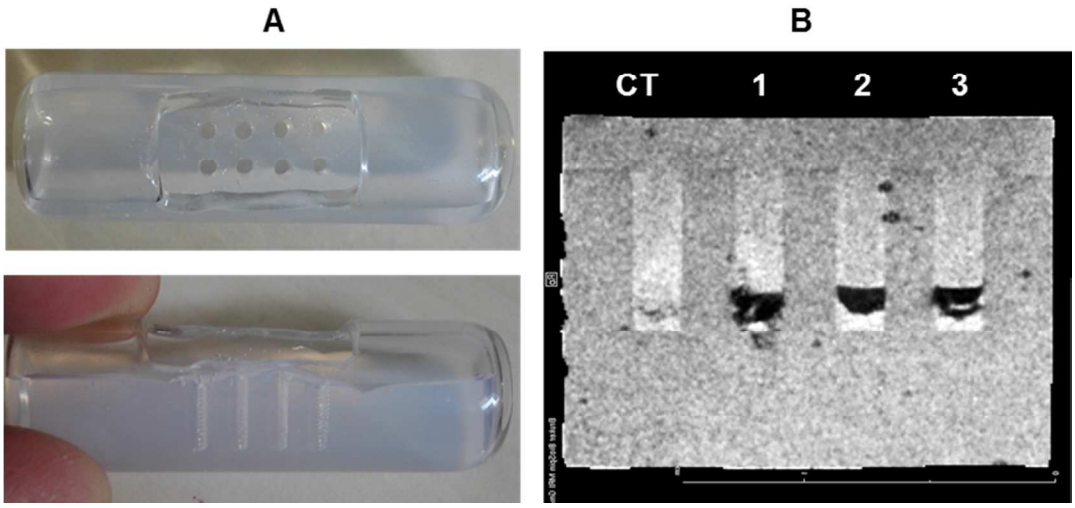


Figure 8. A) Home-made glass cylinder filled with 1% low-melting agarose gel displaying eight small wells dug with a plastic comb (top and lateral views). B) T2* map MR images of Meso 11 control cells (CT), and cells incubated with magneto-fluorescent nanoassemblies **NA-1**, **NA-2** and **NA-3** for 24 h.

Extension to labelling 3D cancer spheroids

Although biological investigations using cell monolayers represent the first compulsory step before envisaging any *in vivo* extensions, they still suffer from severe limitations, especially in the case of cancer treatment. First, the culture of cell monolayers is an artificial model that does not properly reproduce the growth and adhesion conditions of tumor cells *in vivo*. Second, solid tumors are made of compact cell clusters, preventing deep diffusion of the examined drugs. Hence, a novel culture mode of cells in three dimensions (3D), called multicellular tumor cell spheroid (MCTS), is nowadays boosting considerable attention to better apprehend the *in vivo* pathophysiological growing conditions[62] and generate 3D complex artificial tissues.[63] MTCS result from the assembling of 2×10^4 cells, creating a spherical structure of densely packed cells with no adhesion on the surrounding culture material. Phenotype modifications are inevitably

induced and may considerably impact the cellular uptake mechanism. We thus elaborated MTCS out of the Meso 11 mesothelioma cell lines and incubated them with a larger amount of magneto-fluorescent nanoassemblies (40-60 μmol.L^{-1} iron concentration) to take into account the high cell density within the 3D cell arrangements. After usual washing steps and nucleus staining with Hoechst, confocal fluorescence imaging was performed. Reconstituted images from Z-stack acquisitions allowed us to visualize the compact spherical cell organization of MTCS and assess their diameter to be around 400 μm. Bright red-emissive spots could only be seen in the treated spheroids, and could logically be assigned to the magneto-fluorescent nanoassemblies (Figure 9A). Due to the high cell density and large thickness of MTCS, no light transmission could pass through (Figure S11), hence no emission could be collected out of the spheroid centre. Therefore, the images of spheroid equatorial planes may be confusing as the cells in the middle of the structure form a quenched black hole surrounded by a shell of labelled cells (Figure 9B).

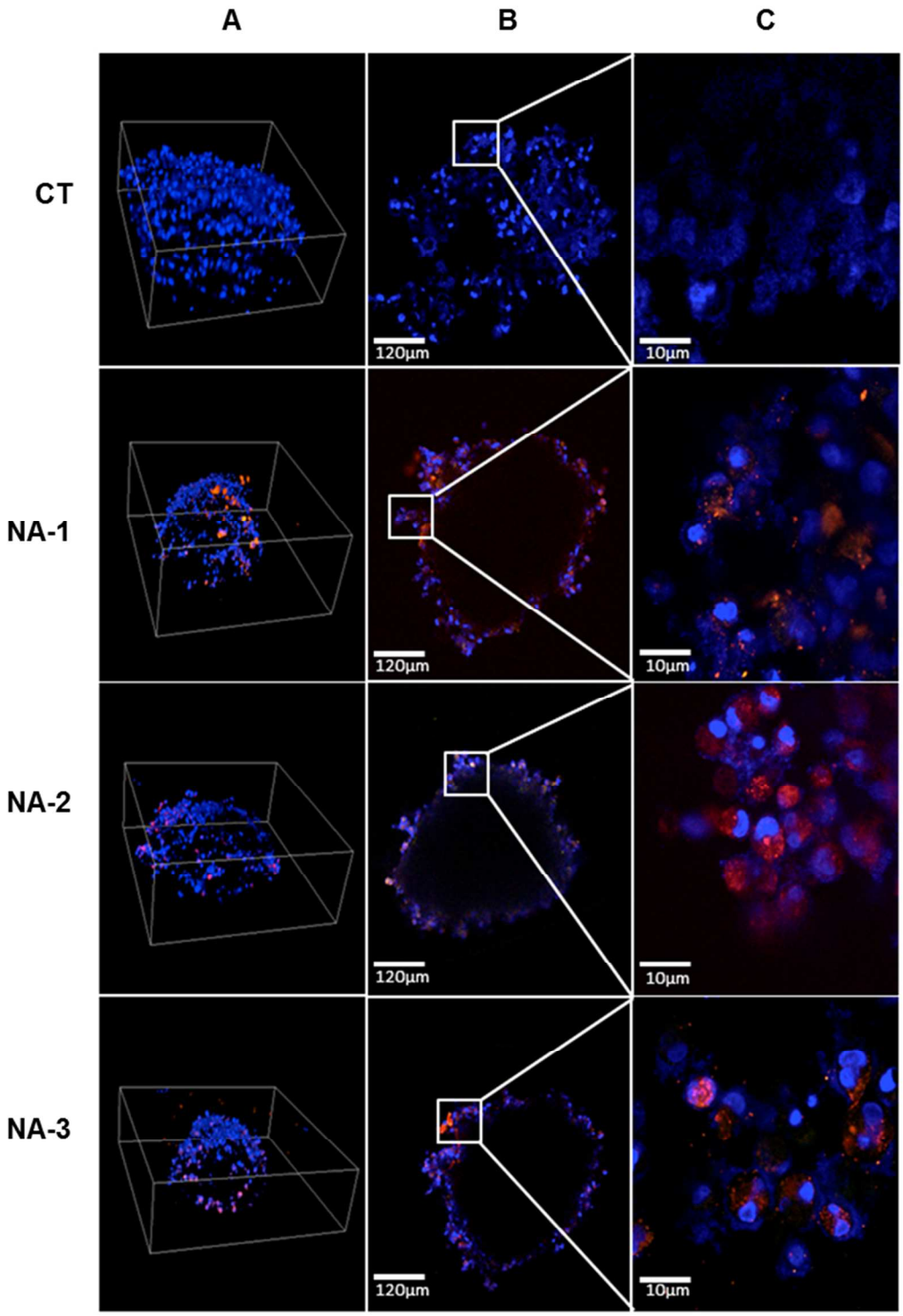


Figure 9. Confocal fluorescence imaging of Meso 11 MTCS (~2×10^4 cells) incubated with magneto-fluorescent nanoassemblies **NA-1**, **NA-2** and **NA-3** for 24 h, and suspended in PBS solution. A) 3D reconstitutions of Z-multistack acquisitions. B) Sections of the spheroid

equatorial planes. C) Magnification of the peripheral shell of Meso 11 cells (blue emissive Hoechst-stained nuclei (λ_{exc} = 405 nm, λ_{em} = 425-475 nm), red-emissive magneto-fluorescent NAs (λ_{exc} = 488 nm, λ_{em} = 570-620 nm).

Magnification of the shell areas provides strong intracellular staining by all three kinds of magneto-fluorescent NAs (Figure 9C). These quite remarkable images point out the fact that our multimodal nanoassemblies are again well-internalized in self-assembled cells and represent bright emissive nanotrackers without blurring the emission of other stained areas thanks to their spot-like signals. Complementary MRI experiments following the same protocol as that described above and using a T2* sequence revealed again notable MRI negative contrast (Figure S12). Compared to the experiments performed on free Meso 11 cells, the reduced response originates from the nanotracker's uptake, limited to the periphery cells, as nicely illustrated by confocal fluorescence imaging.

Before concluding these studies, a natural question arising from these investigations relies on the biodegradability of FON@mag nanoassemblies to serve as future *in vivo* trackers. It is worth recalling that their structure is based on the non-covalent association between three components (a fluorescent core made of small self-assembled molecules, iron oxide nanoparticles, and finally biodegradable polyelectrolytes) through electrostatic interactions, hydrogen bonding or π–π interactions. The absence of covalent linkage should thus easily lead to the natural dissembling over time of all three components as already evidenced in a recent study, hence biodegradability is ruled by each constitutive units. It turns out that iron oxide nanoparticles have recently been proved, through systematic TEM investigations, to undergo progressive destruction and assimilation by the "iron chain" involving ferritin (in charge of

loading iron) and ferroportin (in charge of exporting iron) living media.[6-7,64] As for FONs, the supramolecular association of their hydrophobic fluorophores, mainly driven by van der Waals interactions and hydrogen bonding, progressively leads to the dissolution of the core into individual molecules upon interaction with the lipid membrane of the endosomal/lysosomal compartments where FONs or FON@mag accumulate.[18,45-46] Such dissolution could be demonstrated through the dramatic fluorescence shift from red to greenish as a result of differentiated surroundings of the solvatochromic fluorophores, which could only be explained by changes in solvation and polarity as a result of FON dissociation. All these elements open attractive potentialities for further *in vivo* use since biodegradability and not only biocompatibility has nowadays become a mandatory criteria to meet.

CONCLUSIONS

In this study, we have demonstrated the modular fabrication of high-density core-shell magneto-fluorescent nanoassemblies whose stabilizing external coating only takes place in a final step. In this way, the incidence of the charge density, the chemical nature of the chelating anionic units, the structure, the hydrophobicity and the length of the polyelectrolytes could be independently studied without impacting the general core-shell architecture of the self-assembled magneto-fluorescent probes. Long polyanionic chains (n ≈ 50 repetitive units) or block copolymers revealed unsuccessful to stabilize the ~100 nm-large nanoassemblies due to inter-assembly bridging. By contrast, comb-like polyelectrolytes, comprising short anionic main chains (n ≈ 25 repetitive units) based on poly(methyl methacrylate, brought remarkable colloidal stability. Interestingly, replacing acrylate units with phosphonate ones destroyed the shell of iron oxide

nanoparticles around the FON core, leading to naked FONs. These results emphasize the clear advantage of using polyelectrolytes instead of small anionic ligands thanks to their intrinsic multifold attachment, provided that they do not exert detrimental competitive interactions with the outer shell. Compared to conventional radical polymerization, RAFT-controlled radical polymerization yielded polyelectrolytes with a narrow chain length dispersion. Incorporation of alkyl RAFT agents induced local hydrophobic effects at the nanoassembly surface, generating a more compact solvated structure. In this way, restricted water diffusion to the NA surface is caused by the alkyl chains of the RAFT-controlled polyelectrolytes, which predominantly affects the longitudinal relaxivity r_1 of the resulting magneto-fluorescent nanoassemblies and provides enhanced MRI contrast through r_2/r_1 values as high as 21 at 60 MHz clinical frequency. The lipophilicity and tight organization of the alkyl chains at the nanoassembly surface are also suspected to influence the nanoassembly internalization rate in mesothelioma cancer cells, which showed more progressive uptake without notable cytotoxicity. Labelling of MTCS, resulting from the compaction of thousands of mesothelioma cancer cells could also be performed with all nanoassemblies whose dual-mode MRI and fluorescence imaging capabilities were proved effective. Further investigations on these magneto-fluorescent nanoassemblies displaying easily tunable surface modification are under way to gain insight into the uptake mechanism, *in vivo* distribution and biodegradation as a function of the polyelectrolyte coating that requires accurate control, like those issued from RAFT polymerization, before any clinical transfer can be envisaged.

EXPERIMENTAL SECTION

Polymer synthesis and characterizations

Materials. Azobisisobutyronitrile (AIBN; Sigma-Aldrich; 98 %) was recrystallized twice from methanol prior to use. [(2-methylacryloyl)oxy]methyl phosphonic acid (MAPA) was purchased from Specific Polymers ("MPAC1 Acid") and used as received. Poly(acrylic acid) (PAA) (average M_n 1800 g.mol^{-1}), poly(ethylene glycol) methyl ether methacrylate (average M_n 1100, and average M_n 2000 g.mol^{-1} at 50 wt. % in H_2O; $MAPEG_{1100}$ and $MAPEG_{2000}$, respectively), methacrylic acid (MAA; 99 %) and 2-cyano-2-propyl dodecyl trithiocarbonate (CPDTC; 97 %) were purchased from Sigma-Aldrich and used as received. Polymethacrylic acid (PMMA) homopolymer TP942 (M_w = 6218g.mol^{-1}, M_n = 2609 g.mol^{-1}) was purchased from Coatex Company. Poly(ethylene glycol) methyl ether (PEG_{2000}) (M_w = 2000 g.mol^{-1}) was purchased from Clarian Co, LTD. Methanol (Fischer; 99.5 %) was used as received. N,N-dimethylformamide (DMF; Alfa Aesar; 99.8 %) was distilled under reduced pressure over CaH_2 prior to use.

Synthesis of PMAA-g-PEG_{2000} (**2**). 50 g of PMMA were placed in a four-neck flask and mixed with 0.34 g of a 50 wt. % NaOH solution (corresponding to 2.5 mole % of PMMA carboxylic functions). To the medium were added 95.76 g (corresponding to 29 mole % of PMMA carboxylic functions) of PEG_{2000} and the reaction mixture was heated to 80°C and gradually placed under vacuum (~ 50 mbar). After distillation of water, the temperature of the reaction mixture was gradually increased to 175°C. The reaction time was measured from the moment on the reaction medium reached 170° C. The reaction was continued for a further 4 h. After completion of the reaction, the reaction vessel was returned to atmospheric pressure and the heat turned off. Once the temperature of the reaction mixture reached 90°C, the melted

polymer was diluted to 50 wt. % in water. The polymer was purified by dialysis against distilled water using a dialysis membrane with 3500–5000 molecular weight cut-off (Spectra/Por®2, Spectrum Medical Industries, Inc., CA, USA) at 20°C. The polymer was obtained after lyophilization. The yield of the esterification reaction was controlled by measuring the acidic index before and after the reaction. The grafting efficiency was evaluated to be 23 % by determining the unreacted carboxylic acid content of coupling polymer with an acid-base titration technique.

Synthesis of poly(MAA-stat-MAPEG$_{2000}$) (**3**). The targeted molar fraction in MAA was 80 %. 14 mg of AIBN (8.5×10^{-2} mmol), 55.5 mg of CPDTC (1.61×10^{-2} mmol), 344 mg of MAA (4.00 mmol), 2.0 mL of methanol and 4.00 g of the solution of MAPEG$_{2000}$ at 50 wt. % in water (1.00 mmol) were added in this order into a dried Schlenk flask. The solution was thoroughly deoxygenated by four freeze-pump-thaw cycles. The flask was filled with nitrogen gas and placed in an oil bath maintained at 70 °C for 24 h under magnetic stirring. The solvents were then evaporated under reduced pressure. Analysis by ^{1}H NMR confirmed the almost total conversion of the methacrylate functional groups (> 99 %). The molecular weight of the sample was determined by size exclusion chromatography in DMF.

Synthesis of poly(MAPA-stat-MAPEG$_{1100}$) (**4**). Two samples were synthesized, with targeted molar fractions of MAPA of either 20 % or 60 %. For the synthesis of the former, 3.9 mg of AIBN (0.25 eq.), 32.6 mg of CPDTC (9.44×10^{-2} mmol, 1 eq.), 85.0 mg of MAPA (5 eq.), 2.0768 g of MAPEG$_{1100}$ (20 eq.) and 5.0 mL of DMF were added in this order into a dried Schlenk flask. The solution was thoroughly deoxygenated by four freeze-pump-thaw cycles. The flask was filled with nitrogen gas and placed in an oil bath maintained at 70 °C for 24 h under magnetic stirring. The solvent was then evaporated under reduced pressure. The experimental

procedure was the same for the synthesis of the second sample, with the following proportions for the reactants: 7.8 mg of AIBN (0.25 eq.), 65.3 mg of CPDTC (1.89×10^{-1} mmol, 1 eq.), 510.0 mg of MAPA (15 eq.), 2.0768 g of $MAPEG_{1100}$ (10 eq.) and 5.0 mL of DMF. Analysis by ^{1}H NMR confirmed the almost total conversion of the methacrylate functional groups (> 99 %). The molecular weights of the samples were determined by size exclusion chromatography in DMF.

SEC polymer characterizations. Molecular weights were determined by size exclusion chromatography in DMF containing LiBr at a concentration of 10 $mmol.L^{-1}$. Solutions of samples with concentrations around 5 $mg.mL^{-1}$ were prepared and filtered (PTFE membrane; 0.20 µm) before injection. The flow rate was 0.9 $mL.min^{-1}$ (50 °C). The following Agilent 1260 Infinity series setup was used: a G1310B isocratic pump; a G1322A degasser; a G1329B auto-sampler; a G1316A thermostated column compartment equipped with set of Polymer Laboratories PLgel columns (nominal particle size: 5 µm) composed of a guard column (50×7.5 mm) and two MIXED-D columns (300×7.5 mm); a G1314B variable wavelength detector; a G7800A multidetector suite equipped with a MDS refractive index detector. Calibration was performed using a set of EasiVial polystyrene PS-M standards. Agilent GPC/SEC software and multi-detector upgrade were used to determine molar mass values and distributions.

Fabrication and structural characterizations of polyelectrolyte-coated nanoassemblies

Nanoassembly fabrication. A solution of phosphonic acid fluorophores,[17] dissolved in THF (50 µL, 0.1 wt. %) was added under vigorous stirring to a solution of maghemite nanoparticles in nitric acid (2.5 mL, 0.006 wt. %, pH = 1.2). After a few seconds, the magneto-fluorescent NAs were formed. The polyelectrolyte of interest was added as a powder (added amount for PAA (**1**): 5 mg, PMAA-*g*-PEG (**2**): 17 mg, and poly(MAA-*stat*-MAPEG) (**3**): 18 mg) and then, ammonium hydroxide ($1\ mol.L^{-1}$) was added dropwise under stirring until pH = 9 was reached.

The resulting translucent solution was allowed to stir for a further 30 min and dialyzed using a Spectra Por membrane (Standard Grade Regenerated Cellulose; cut-off: 8-10 kDa for PAA (**1**), and 300 kDa for (**2**) and (**3**) against Millipore water (600 mL) over 24 h to remove the excess of polymers and get neutral pH. The resulting solution was spread into small vials (2 mL content) and lyophilized. The vials were finally stored at -18 °C until solution reconstitution with water, PBS or cell culture medium.

DLS characterizations. The hydrodynamic diameter D_H and size dispersion of the nano-objects were determined by dynamic light scattering (DLS) by means of a nanoparticle size analyzer Cordouan (Vasco 3) equipped with a 40 mW diode laser operating at 658 nm. Measurements were collected in a backscattering mode at an angle of 135°. Measurements were carried out at 25 °C on aqueous solutions of NPs. For each sample, intensity measurements were carried out in a multi-acquisition mode implying automatically adjusted correlograms, and averaged measurements on 6 acquisitions. Nanoparticle mean sizes and distribution widths were obtained by fitting each correlogram with a Cumulants algorithm. Measurements of surface potential ζ were carried out by means of a Zetasizer Nano ZS ZEN 3600 (Malvern). The samples were placed in quartz cells. Several measurements were realized for each sample according to a predefined operating procedure.

TEM analyses. Nanoparticle morphology was investigated by transmission electron microscopy (MO-Jeol 123S0 (80 kV)). All NA solutions were deposited onto holey carbon-coated copper grids (300 mesh).

Steady-state and time-resolved fluorescence measurements

Steady-state fluorescence measurements. UV-visible absorption spectra were recorded using a Varian Model Cary 5E spectrophotometer equipped with an integrating sphere DRA

2500. Fluorolog 2 spectrofluorimeter was used (Jobin-Yvon/Horiba). Correction for the emission spectra with regard to the spectral response of the detector was automatically applied. Fluorescence quantum yields were determined in solution, referred to coumarine 540 A in EtOH ($\Phi_f = 0.38$).[65]

Time-resolved fluorescence measurements. Fluorescence time decays were measured in water using the fully automated spectrofluorimeter (model Fluotime 300, PicoQuant) following the time-correlated photon counting method. Excitation was performed using a pulsed laser diode (LDH-D-C-450B) working at 450 ± 10 nm with a 70 ps full width at half maximum. The excitation and emission polarizers were set in the vertical position and at the magic angle (54.7°) respectively to get polarization-independent fluorescence signals Fluorescence decays were recorded using a Hybrid-PMT detector combined with an acquisition temporal resolution up to 25 ps. A 473 nm Notch filter (BPL01-473R-25) purchased from Semrock was used to discard any possible contribution of excitation light scattering).

Static and dynamic magnetic measurements

Magnetization measurements. Magnetic measurements were collected with a Quantum Design MPMS-5S SQUID magnetometer. All magnetic measurements were performed on dry powders. The samples were pressed into pellets in order to prevent nanocrystal orientation under the external magnetic field. The magnetization curves were measured at 2.5 K and 310 K from +50 kOe to -50 kOe. All data were corrected for diamagnetic contribution due to the sample holder which was separately measured. The thermal dependence of magnetization was recorded from 10 to 300 K upon zero-field-cooling (ZFC) and field-cooling (FC) conditions. ZFC magnetizations were measured by cooling samples in a zero magnetic field and then by

increasing the temperature in the presence of a 50 Oe magnetic field, whereas field-cooled (FC) curves were recorded by cooling the samples in the same probe field at 50 Oe.

NMR relaxometry measurements. Measurements of ^{1}H NMR longitudinal (T_1) and transverse (T_2) relaxation times were performed at room temperature on sample solutions diluted with water in the range 0.01 MHz $\leq \upsilon \leq$ 60 MHz frequency range. Generation and detection of the NMR signal involved a Smartracer Stelar relaxometer (using the Fast-Field-Cycling technique) for $\upsilon \leq$ 10 MHz, and a Stelar Spinmaster spectrometer for $\upsilon >$ 10 MHz. For the very low field range ($\upsilon <$ 3.2 MHz for T_1 and $\upsilon <$ 4 MHz for T_2), ad hoc pre-polarized sequences were used to increase the NMR proton signal. In the second case, the standard radio frequency excitation sequences Carr-Purcell-Meiboom-Gill (CPMG)-like (T_2) and saturation recovery (T_1) were used. The efficiency of samples as MRI contrast agents was determined from the measured T_1 and T_2 by calculating the nuclear longitudinal r_1 and transverse r_2 relaxivities as given by:

$$r_i = \frac{(1/T_i)_{meas} - (1/T_i)_{dia}}{c_{Fe}}$$

where $(1/T_i)_{meas}$ is the measured relaxation rate, $(1/T_i)_{dia.}$ the diamagnetic contribution of Millipore water (~ 4 s^{-1}), and c_{Fe} the iron concentration in mmol.L^{-1} for each sample.

Photophysical characterizations. UV-visible absorption spectra were recorded using a Varian Model Cary 5E spectrophotometer equipped with an integrating sphere DRA 2500. Fluorolog 2 spectrofluorimeter was used (Jobin-Yvon/Horiba). Correction for the emission spectra with regard to the spectral response of the detector was automatically applied. Fluorescence quantum yields were determined in solution, referred to coumarine 540 A in EtOH (Φ_f = 0.38).[65]

Cell culture, internalization and bioimaging

Cell culture. The mesothelioma cell line Meso 11 was established from pleural fluids of patients. All cells were maintained in RPMI medium (Invitrogen) supplemented with 2 $mmol.L^{-1}$ glutamine, 100 IU/mL penicillin, 0.1 $mg.mL^{-1}$ streptomycin and 10 % heat-inactivated fœtal calf serum(FCS)(Eurobio), and grown in a humidified atmosphere of 37 °C and 5 % CO_2. For all experiments, the cell cultures at a confluence of about 80–90 % were washed once with phosphate buffered saline (PBS) and trypsinized (0.05 % trypsin/0.02 % EDTA)(Invitrogen) for 5 minutes. The cells were re-suspended in culture medium and eosin was used to determine viability before seeding.

Three-dimensional (3D) spheroid culture. Meso 11 cells were seeded into Nunclon Sphera 96-well microplate (Thermoscientific) at a density of 2×10^4 cells/well in 180 µL of culture medium. Cells were centrifuged at 800 G for 1 minute. After 48 h of incubation at 37°C and 5 % CO_2, the 3D spheroid structure was established.

Flow cytometry studies. Meso 11 cells were seeded on a 6-well plate at 2×10^5 cells per well. After 24 h, solutions of **NA-1**, **NA-2** and **NA-3** (final iron concentration of 3.3 $\mu mol.L^{-1}$, 2.6 $\mu mol.L^{-1}$ and 2.09 $\mu mol.L^{-1}$) were added and let in contact for 30, 60, 120, 240, 360, 960 and 1440 minutes. Then, each well was washed with PBS and incubated with 300 µL of trypsin/EDTA for 5 minutes. 700 µL of culture medium were added and the cell suspensions were centrifuged at 800 G for 5 minutes. The cell pellets were re-suspended in PBS (50 µL) containing Zombie NIR® (Biolegend) diluted at 1/50 and incubated 30 minutes at room temperature. Analyses were performed using an ImageStreamX Imaging Flow Cytometer (Amnis Corporation, Seattle, WA) equipped with INSPIRE software. A 40× magnification was used for all samples. 10^4 living cells were analyzed for each conditions. Data analysis was

performed using the IDEAS software (Amnis Corporation). The nanoassemblies and Zombie NIR® were excited with a 488 nm ion-argon laser (power 100 mW). Fluorescence signals of the nanoassemblies and Zombie NIR® were collected on channel 3 (560-595 nm and channel 12 (745-800 nm), respectively. Intensity-adjusted brightfield images were collected on channel 1 (430-480 nm). The gating strategy for analysis involved the selection of focused live cells first on viability marker, then on the nanoassembly fluorescence.

Cell monolayer fixation and TEM imaging. Meso 11 cells were seeded on a 6-well plate at 5×10^5 cells per well. After 24 h, solutions of **NA-1**, **NA-2** and **NA-3** (final iron concentration of 3.3 $\mu mol.L^{-1}$, 2.6 $\mu mol.L^{-1}$ and 2.09 $\mu mol.L^{-1}$, respectively) were added and let in contact for 24 h. The cells were washed with phosphate buffer (5 mL), and fixed in phosphate buffer 1 $\mu mol.L^{-1}$ containing 1.6 % glutaraldehyde for 1 h at 4°C. They were washed with 0.1 $mol.L^{-1}$ phosphate buffer at pH 7.2 (0.5 mL) and post-fixed in 1 % osmium tetraoxide and cacodylate buffer for 1h at 4 °C. After fixation, the samples were rinsed with cacodylate buffer and dried with increasing concentrations of ethanol and propylene oxide, embedded in EMBed-812 resin (Agar Scientific, UK) and further polymerized. The resulting embedded cells were cut with an UltraCut E microtome (Leica, Wetzlar, Germany) and placed onto copper grids. TEM observation of grids was performed using a JEM-1010 microscope (JEOL, Tokyo, Japan), operating at an accelerated voltage of 100 kV.

Confocal fluorescence and transmission microscopy. Confocal fluorescence imaging was performed using a Nikon A1R Si microscope, equipped with Ar^+ and He-Ne lasers as excitation sources and an oil-immersion objective Plan Apo, 60×, NA = 1.4). Transmission imaging were obtained using an Axio Observer.Z1 Zeiss microscope using two distinct objectives (oil-immersion objective: A Pln, 63×, NA = 1.4, DICIII; objective A Pln 40×, 0.5 Ph_2). Cell imaging:

Meso 11 cells were seeded on a µ-slide 8-well ibitreat microscopy chamber (Ibidi). After 24 h, solutions of **NA-1**, **NA-2** and **NA-3** (final iron concentration of 3.3 µmol.L^{-1}, 2.6 µmol.L^{-1} and 2.09 µmol.L^{-1}, respectively) were added and let in contact for 24 h. Each well was washed with PBS and incubated with 5 µg.mL^{-1} WGA Alexa Fluor® 647 conjugate for 10 min at 37°C. The cells were then washed twice with PBS and incubated with 5 µg.mL^{-1} Hoechst for nucleus staining and 4 % paraformaldehyde for 15 minutes. Spheroid imaging: Meso 11 spheroids were treated with **NA-1**, **NA-2** and **NA-3** (final iron concentration of 65.7 µmol.L^{-1}, 52.2 µmol.L^{-1} and 41.7 µmol.L^{-1}, respectively) for 24 h. Each well was washed with PBS and incubated with 5 µg.mL^{-1} Hoechst for nucleus staining and 4 % paraformaldehyde for 15 minutes. Meso 11 MTCS were washed once with PBS and transferred into µ-slide angiogenesis plate (Ibidi) for imaging.

Magnetic resonance imaging of cell monolayers and spheroids. A scaffold was designed according to a glass cylinder (54 mm × 27 mm). The ghost background was filled by 1% low-melting agarose gel (type I - Sigma-Aldrich) and two rows of four wells were created thanks to a plastic comb designed by a 3D printer. Monolayers of Meso 11 cells were seeded in the first row's wells at a density of 2 $\times 10^4$ cells/well in PBS. Sixteen Meso 11 MTCS were seeded on each second row's well. The top of the scaffold was filled by 1 % low-gelling agarose gel (type I - Sigma-Aldrich). All MRI studies were performed with a Biospec Avance III MR scanner (Bruker Biospin, Wissembourg, France) using a 20 cm bore 7 T magnet equipped with BGA12S gradient/ shim system capable of 675 mT.m^{-1} maximum gradient strength. A 35-mm-diameter volume coil was used.

ASSOCIATED CONTENT

Supporting Information. SDS-PAGE and magnetophoresis protocols and additional TEM, photophysical and MRI characterizations. This material is available free of charge via the Internet at http://pubs.acs.org.

AUTHOR INFORMATION

Corresponding Author

*E-mail: elena.ishow@univ-nantes.fr – Phone: +33-2-5112-5375.

*E-mail: christophe.blanquart@univ-nantes.fr – Phone: +33-2-2808-0238.

*E-mail : julien.poly@uha.fr – Phone: +33-3-8960-8802.

Author Contributions

The manuscript was written through contributions of all authors. All authors have given approval to the final version of the manuscript.

Funding Sources

The “Ligue contre le cancer 44” is gratefully acknowledged for their strong support as well as CNRS through its “Mission pour l’Interdisciplinarité” board (program “Nano Challenge: Health and Welfare” / ETHICAM project) and its France-Italy partnership (program PICS / MOCACINO project), and Région des Pays de la Loire through the PhD program of LUMOMAT RFI (ONASSIS project).

ACKNOWLEDGEMENT

We deeply acknowledge Carole La (LPGN, UMR CNRS 6112 – Université Nantes), Brigitte Bouchet (INRA Nantes-Angers), andEric Gautron (IMN, UMR 6502 – Université Nantes), Louis Ryo and François-Xavier Lefèvre (CEISAM, UMR CNRS 6230 – Université Nantes), Florence

Franconi (PIAM- Angers), Thierry Guizouarn (ISCR, UMR CNRS 6226 – Université de Rennes 1), Juliette Desfrançois (Plateforme CytoCell, INSERM UMR 1232, Nantes), Florence Gazeau and Claire Wilhelm (MSC, UMR CNRS 7057 – Université Paris Diderot), Jérôme Fresnais (PHENIX, UMR CNRS 8234 - Université Pierre et Marie Curie), for ICP-OES iron titrations, access to TEM platform, glass blowing and SEM measurements, MRI measurements, SQUID measurements, flow cytometry, access to magnetophoresis facilities, and for providing acidic solutions of SPIONs, respectively.

REFERENCES

(1) Prado, Y.; Daffe, N.; Michel, A.; Georgelin, T.; Yaacoub, N.; Greneche, J.-M.; Choueikani, F.; Otero, E.; Ohresser, P.; Arrio, M.-A.; Cartier-dit-Moulin, C.; Sainctavit, P.; Fleury, B.; Dupuis, V.; Lisnard, L.; Fresnais, J. Enhancing the magnetic anisotropy of maghemite nanoparticles via the surface coordination of molecular complexes. *Nat Commun* **2015**, *6*.

(2) de Boer, P.; Hoogenboom, J. P.; Giepmans, B. N. G. Correlated Light and Electron Microscopy: Ultrastructure Lights Up! *Nat. Methods* **2015**, *12*, 503-513.

(3) Feld, A.; Merkl, J.-P.; Kloust, H.; Flessau, S.; Schmidtke, C.; Wolter, C.; Ostermann, J.; Kampferbeck, M.; Eggers, R.; Mews, A.; Schotten, T.; Weller, H. A Universal Approach to Ultrasmall Magneto-Fluorescent Nanohybrids. *Angew. Chem., Int. Ed.* **2015**, *54*, 12468-12471.

(4) Chen, O.; Riedemann, L.; Etoc, F.; Herrmann, H.; Coppey, M.; Barch, M.; Farrar, C. T.; Zhao, J.; Bruns, O. T.; Wei, H.; Guo, P.; Cui, J.; Jensen, R.; Chen, Y.; Harris, D. K.; Cordero, J. M.; Wang, Z. W.; Jasanoff, A.; Fukumura, D.; Reimer, R.; Dahan, M.; Jain, R.

K.; Bawendi, M. G. Magneto-Fluorescent Core-Shell Supernanoparticles. *Nat. Commun.* **2014**, *5*, 5093.

(5) Reddy, L. H.; Arias, J. L.; Nicolas, J.; Couvreur, P. Magnetic Nanoparticles: Design and Characterization, Toxicity and Biocompatibility, Pharmaceutical and Biomedical Applications. *Chem. Rev.* **2012**, *112*, 5818-5878.

(6) Mazuel, F.; Espinosa, A.; Luciani, N.; Reffay, M.; Le Borgne, R.; Motte, L.; Desboeufs, K.; Michel, A.; Pellegrino, T.; Lalatonne, Y.; Wilhelm, C. Massive Intracellular Biodegradation of Iron Oxide Nanoparticles Evidenced Magnetically at Single-Endosome and Tissue Levels. *ACS Nano* **2016**, *10*, 7627-7638.

(7) Lartigue, L.; Alloyeau, D.; Kolosnjaj-Tabi, J.; Javed, Y.; Guardia, P.; Riedinger, A.; Péchoux, C.; Pellegrino, T.; Wilhelm, C.; Gazeau, F. Biodegradation of Iron Oxide Nanocubes: High-Resolution In Situ Monitoring. *ACS Nano* **2013**, *7*, 3939-3952.

(8) Gupta, A. K.; Gupta, M. Synthesis and Surface Engineering of Iron Oxide Nanoparticles for Biomedical Applications. *Biomaterials* **2005**, *26*, 3995-4021.

(9) Lee, P.-W.; Hsu, S.-H.; Wang, J.-J.; Tsai, J.-S.; Lin, K.-J.; Wey, S.-P.; F.-R., C.; Lai, C.-H.; Yen, T.-C.; Sung, H.-W. The Characteristics, Biodistribution, Magnetic Resonance Imaging and Biodegradability of Superparamagnetic Core–Shell Nanoparticles. *Biomaterials* **2010**, *1316-1324*, 1316-1324.

(10) Laurent, S.; Forge, D.; Port, M.; Roch, A.; Robic, C.; Vander Elst, L.; Muller, R. N. Magnetic Iron Oxide Nanoparticles: Synthesis, Stabilization, Vectorization, Physicochemical Characterizations, and Biological Applications. *Chem. Rev.* **2008**, *108*, 2064-2110.

(11) Vuong, Q. L.; Berret, J. F.; Fresnais, J.; Gossuin, Y.; Sandre, O. A Universal Scaling Law to Predict the Efficiency of Magnetic Nanoparticles as MRI T2-Contrast Agents. *Adv. Healthcare Mater.* **2012**, *1*, 502-512.

(12) Paquet, C.; de Haan, H. W.; Leek, D. M.; Lin, H. Y.; Xiang, B.; Tian, G. H.; Kell, A.; Simard, B. Clusters of Superparamagnetic Iron Oxide Nanoparticles Encapsulated in a Hydrogel: A Particle Architecture Generating a Synergistic Enhancement of the T-2 Relaxation. *ACS Nano* **2011**, *5*, 3104-3112.

(13) Hickey, R. J.; Koski, J.; Meng, X.; Riggleman, R. A.; Zhang, P. J.; Park, S. J. Size-Controlled Self-Assembly of Superparamagnetic Polymersomes. *ACS Nano* **2014**, *8*, 495-502.

(14) Béalle, G.; Di Corato, R.; Kolosnjaj-Tabi, J.; Dupuis, V.; Clément, O.; Gazeau, F.; Wilhelm, C.; Ménager, C. Ultra Magnetic Liposomes for MR Imaging, Targeting, and Hyperthermia. *Langmuir* **2012**, *28*, 11834-11842.

(15) Casula, M. F.; Floris, P.; Innocenti, C.; Lascialfari, A.; Marinone, M.; Corti, M.; Sperling, R. A.; Parak, W. J.; Sangregorio, C. Magnetic Resonance Imaging Contrast Agents Based on Iron Oxide Superparamagnetic Ferrofluids. *Chem. Mater.* **2010**, *22*, 1739-1748.

(16) Di Corato, R.; Béalle, G.; Kolosnjaj-Tabi, J.; Espinosa, A.; Clément, O.; Silva, A. K. A.; Ménager, C.; Wilhelm, C. Combining Magnetic Hyperthermia and Photodynamic Therapy for Tumor Ablation with Photoresponsive Magnetic Liposomes. *ACS Nano* **2015**, *9*, 2904-2916.

(17) Faucon, A.; Fresnais, J.; Brosseau, A.; Hulin, P.; Nedellec, S.; Hemez, J.; Ishow, E. Photoactive Chelating Organic Nanospheres as Central Platforms of Bimodal Hybrid Nanoparticles. *J. Mater. Chem. C* **2013**, *1*, 3879-3886.

(18) Faucon, A.; Benhelli-Mokran, H.; Fleury, F.; Dubreil, L.; Hulin, P.; Nedellec, S.; Doussineau, T.; Antoine, R.; Orlando, T.; Lascialfari, A.; Fresnais, J.; Lartigue, L.; Ishow, E. Tuning the Architectural Integrity of High-Performance Magnetofluorescent Core-Shell Nanoassemblies in Cancer Cells. *J. Colloid Interface Sci.* **2016**, *479*, 139–149.

(19) Fresnais, J.; Berret, J.-F.; Frka-Petesic, B.; Sandre, O.; Perzynski, R. Electrostatic Co-Assembly of Iron Oxide Nanoparticles and Polymers: Towards the Generation of Highly Persistent Superparamagnetic Nanorods. *Adv. Mater.* **2008**, *20*, 1-5.

(20) Chanteau, B.; Fresnais, J.; Berret, J. F. Electrosteric Enhanced Stability of Functional Sub-10 nm Cerium and Iron Oxide Particles in Cell Culture Medium. *Langmuir* **2009**, *25*, 9064-9070.

(21) Kadajji, V. G.; Betageri, G. V. Water Soluble Polymers for Pharmaceutical Applications. *Polymers* **2011**, *2*, 1972-2009.

(22) Faucon, A.; Maldiney, T.; Clément, O.; Hulin, P.; Nedellec, S.; Robard, M.; Gautier, N.; De Meulenaere, E.; Clays, K.; Orlando, T.; Lascialfari, A.; Fiorini-Debuisschert, C.; Fresnais, J.; Ishow, E. Highly Cohesive Dual Nanoassemblies for Complementary Multiscale Bioimaging. *J. Mater. Chem. B* **2014**, *2*, 7747-7755.

(23) Torrisi, V.; Graillot, A.; Vitorazi, L.; Crouzet, Q.; Marletta, G.; Loubat, C.; Berret, J. F. Preventing Corona Effects: Multiphosphonic Acid Poly(ethylene glycol) Copolymers for Stable Stealth Iron Oxide Nanoparticles. *Biomacromolecules* **2014**, *15*, 3171-3179.

(24) Markiewicz, K. H.; Seiler, L.; Misztalewska, I.; Winkler, K.; Harrisson, S.; Wilczewska, A. Z.; Destarac, M.; Marty, J. D. Advantages of Poly(Vinyl Phosphonic Acid)-Based Double Hydrophilic Block Copolymers for The Stabilization of Iron Oxide Nanoparticles. *Polymer Chem.* **2016**, *7*, 6391-6399.

(25) Verma, A.; Stellacci, F. Effect of surface properties on nanoparticle-cell interactions. *Small* **2010**, *6*, 12-21.

(26) Ashby, J.; Pan, S. Q.; Zhong, W. W. Size and Surface Functionalization of Iron Oxide Nanoparticles Influence the Composition and Dynamic Nature of Their Protein Corona. *ACS Appl. Mater. Interfaces* **2014**, *6*, 15412-15419.

(27) Saha, K.; Rahimi, M.; Yazdani, M.; Kim, S. T.; Moyano, D. F.; Hou, S.; Das, R.; Mout, R.; Rezaee, F.; Mahmoudi, M.; Rotello, V. M. Regulation of Macrophage Recognition through the Interplay of Nanoparticle Surface Functionality and Protein Corona. *ACS Nano* **2016**, *10*, 4421-4430.

(28) Huang, R.; Carney, R. P.; Ikuma, K.; Stellacci, F.; Lau, B. L. T. Effects of Surface Compositional and Structural Heterogeneity on Nanoparticle–Protein Interactions: Different Protein Configurations. *ACS Nano* **2014**, *8*, 5402-5412.

(29) Nasongkla, N.; Chen, B.; Macaraeg, N.; Fox, M. E.; Fréchet, J. M. J.; Szoka, F. C. Dependence of Pharmacokinetics and Biodistribution on Polymer Architecture: Effect of Cyclic versus Linear Polymers. *J. Am. Chem. Soc.* **2009**, *131*, 3842-3843.

(30) Setyawati, M. I.; Tay, C. Y.; Docter, D.; Stauber, R. H.; Leong, D. T. Understanding and Exploiting Nanoparticles' Intimacy with The Blood Vessel and Blood. *Chem. Soc. Rev.* **2015**, *44*.

(31) Ménager, C.; Sandre, O.; Mangili, J.; Cabuil, V. Preparation and Swelling of Hydrophilic Magnetic Microgels. *Polymer* **2004**, *45*, 2475-2481.

(32) Fery-Forgues, S. Fluorescent organic nanocrystals and non-doped particles for biological applications. *Nanoscale* **2013**, *51*, 8428-8437.

(33) Fischer, I.; Petkau-Milroy, K.; Dorland, Y. L.; Schenning, A.; Brunsveld, L. Self-Assembled Fluorescent Organic Nanoparticles for Live-Cell Imaging. *Chem. Eur. J.* **2013**, *19*, 16646-16650.

(34) Bouhamed, H.; Boufi, S.; Magnin, A. Alumina interaction with AMPS-MPEG copolymers produced by RAFT polymerization: Stability and rheological behavior. *J. Coll. Interface Sci.* **2009**, *333*, 209-220.

(35) McCormick, C. L.; Lowe, A. B. Aqueous RAFT Polymerization: Recent Developments in Synthesis of Functional Water-Soluble (Co)polymers with Controlled Structures. *Acc. Chem. Res.* **2004**, *37*, 312-325.

(36) Boyer, C.; Bulmus, V.; Davis, T. P.; Ladmiral, V.; Liu, J.; Perrier, S. Bioapplications of RAFT Polymerization. *Chem. Rev.* **2009**, *109*, 5402-5436.

(37) Tian, J.; Zheng, F.; Zhao, H. Nanoparticles with Fe3O4−Nanoparticle Cores and Gold-Nanoparticle Coronae Prepared by Self-Assembly Approach. *The Journal of Physical Chemistry C* **2011**, *115*, 3304-3312.

(38) Pissuwan, D.; Boyer, C.; Gunasekaran, K.; Davis, T. P.; Bulmus, V. In Vitro Cytotoxicity of RAFT Polymers. *Biomacromolecules* **2010**, *11*, 412–420.

(39) Sumerlin, B. S.; Matyjaszewski, K., Molecular Brushes – Densely Grafted Copolymers. In *Macromolecular Engineering*, Wiley-VCH Verlag GmbH & Co. KGaA: 2007; pp 1103-1135.

(40) Mignot, A.; Truillet, C.; Lux, F.; Sancey, L.; Louis, C.; Denat, F.; Boschetti, F.; Bocher, L.; Gloter, A.; Stephan, O.; Antoine, R.; Dugourd, P.; Luneau, D.; Novitchi, G.; Figueiredo, L. C.; de Morais, P. C.; Bonneviot, L.; Albela, B.; Ribot, F.; Van Lokeren, L.; Dechamps-Olivier, I.; Chuburu, F.; Lemercier, G.; Villiers, C.; Marche, P. N.; Le Duc, G.;

Roux, S.; Tillement, O.; Perriat, P. A Top-Down Synthesis Route to Ultrasmall Multifunctional Gd-Based Silica Nanoparticles for Theranostic Applications. *Chem. Eur. J.* **2013**, *19*, 6122-6136.

(41) Ishow, E.; Faucon, A. Magnetic and Fluorescent Reverse Nanoassemblies. US 14/218,368 - PCT/EP2015/055711, **March 2015**.

(42) Johnson, N. J. J.; He, S.; Hun, V. A. N.; Almutairi, A. Compact Micellization: A Strategy for Ultrahigh T-1 Magnetic Resonance Contrast with Gadolinium-Based Nanocrystals. *ACS Nano* **2016**, *10*, 8299-8307.

(43) Willcock, H.; K. O'Reilly, R. End Group Removal and Modification of RAFT Polymers. *Polym. Chem.* **2010**, *1*, 149-157.

(44) Faucon, A.; Lenk, R.; Hemez, J.; Gautron, E.; Jacquemin, D.; Le Questel, J.-Y.; Graton, J.; Brosseau, A.; Ishow, E. Fluorescent Carboxylic and Phosphonic Acids: Comparative Photophysics from Solution to Organic Nanoparticles. *Phys. Chem. Chem. Phys.* **2013**, *15*, 12748-12756.

(45) Faucon, A.; Benhelli-Mokrani, H.; Córdova, L. A.; Brulin, B.; Heymann, D.; Hulin, P.; Nedellec, S.; Ishow, E. Long-Term Fate of Fluorescent Organic Nanoparticles as Bioimaging Agents in Cancer Cells and Macrophages. *Adv. Health. Mater* **2015**, *4*, 2727-2734.

(46) Breton, M.; Prevel, G.; Audibert, J. F.; Pansu, R.; Tauc, P.; Le Pioufle, B.; Francais, O.; Fresnais, J.; Berret, J. F.; Ishow, E. Solvatochromic Dissociation of Non-Covalent Fluorescent Organic Nanoparticles upon Cell Internalization. *Phys. Chem. Chem. Phys.* **2011**, *13*, 13268-13276.

(47) Farinha, J. P. S.; Relógio, P.; Charreyre, M.-T.; Prazeres, T. J. V.; Martinho, J. M. G. Understanding Fluorescence Quenching in Polymers Obtained by RAFT. *Macromolecules* **2007**, *40*, 4680-4690.

(48) Nandwana, V.; Ryoo, S. R.; Kanthala, S.; De, M.; Chou, S. S.; Prasad, P. V.; Dravid, V. P. Engineered Theranostic Magnetic Nanostructures: Role of Composition and Surface Coating on Magnetic Resonance Imaging Contrast and Thermal Activation. *ACS Appl. Mater. Interfaces* **2016**, *8*, 6953-6961.

(49) Poselt, E.; Kloust, H.; Tromsdorf, U.; Janschel, M.; Hahn, C.; Masslo, C.; Weller, H. Relaxivity Optimization of a PEGylated Iron-Oxide-Based Negative Magnetic Resonance Contrast Agent for T-2-Weighted Spin-Echo Imaging. *ACS Nano* **2012**, *6*, 1619-1624.

(50) Roch, A.; Muller, R. N.; Gillis, P. Theory of Proton Relaxation Induced by Superparamagnetic Particles. *J. Chem. Phys.* **1999**, *110*, 5403-5411.

(51) Ternent, L.; Mayoh, D. A.; Lees, M. R.; Davies, G. L. Heparin-Stabilised Iron Oxide for MR Applications: A Relaxometric Study. *J. Mater. Chem. B* **2016**, *4*, 3065-3074.

(52) Meledandri, C. J.; Ninjbadgar, T.; Brougham, D. F. Size-controlled magnetoliposomes with tunable magnetic resonance relaxation enhancements. *J. Mater. Chem.* **2011**, *21*, 214-222.

(53) Gossuin, Y.; Gillis, P.; Hocq, A.; Vuong, Q. L.; Roch, A. Magnetic Resonance Relaxation Properties of Superparamagnetic Particles. *Wiley Interdiscip. Rev.: Nanomed. Nanobiotechnol.* **2009**, *1*, 299-310.

(54) Vuong, Q. L.; Berret, J.-F.; Fresnais, J.; Gossuin, Y.; Sandre, O. A Universal Scaling Law to Predict the Efficiency of Magnetic Nanoparticles as MRI T2-Contrast Agents. *Adv. Health. Mater.* **2012**, *1*, 502-512.

(55) Meng, H.; Xia, T.; George, S.; Nel, A. E. A Predictive Toxicological Paradigm for the Safety Assessment of Nanomaterials. *ACS Nano* **2009**, *3*, 1620-1627.

(56) Lartigue, L.; Hugounenq, P.; Alloyeau, D.; Clarke, S. P.; Lévy, M.; Bacri, J.-C.; Bazzi, R.; Brougham, D. F.; Wilhelm, C.; Gazeau, F. Cooperative Organization in Iron Oxide Multi-Core Nanoparticles Potentiates Their Efficiency as Heating Mediators and MRI Contrast Agents. *ACS Nano* **2012**, *6*, 10935-10949.

(57) Jansch, M.; Stumpf, P.; Graf, C.; Rühl, E.; Müller, R. H. Adsorption Kinetics of Plasma Proteins on Ultrasmall Superparamagnetic Iron Oxide (USPIO) Nanoparticles. *Int. J. Pharm.* **2012**, *428*, 125-133.

(58) Xia, T.; Kovochich, M.; Liong, M.; Zink, J. I.; Nel, A. E. Cationic Polystyrene Nanosphere Toxicity Depends on Cell-Specific Endocytic and Mitochondrial Injury Pathways. *ACS Nano* **2008**, *2*, 85-96.

(59) Weinstein, J. S.; Varallyay, C. G.; Dosa, E.; Gahramanov, S.; Hamilton, B.; Rooney, W. D.; Muldoon, L. L.; Neuwelt, E. A. Superparamagnetic iron oxide nanoparticles: diagnostic magnetic resonance imaging and potential therapeutic applications in neurooncology and central nervous system inflammatory pathologies, a review. *J. Cereb. Blood Flow Metab.* **2010**, *30*, 15-35.

(60) Wrynna, A. S.; Mac Sweeneya, C. ı. P.; Franconi, F.; Lemaired, L.; Pouliquen, D.; Herlidou, S.; Leonard, B. E.; Gandon, J.-M.; de Certaines, J. D. An In-Vivo Magnetic Resonance Imaging Study of The Olfactory Bulbectomized Rat Model of Depression. *Brain Res.* **2000**, *879*, 193-199.

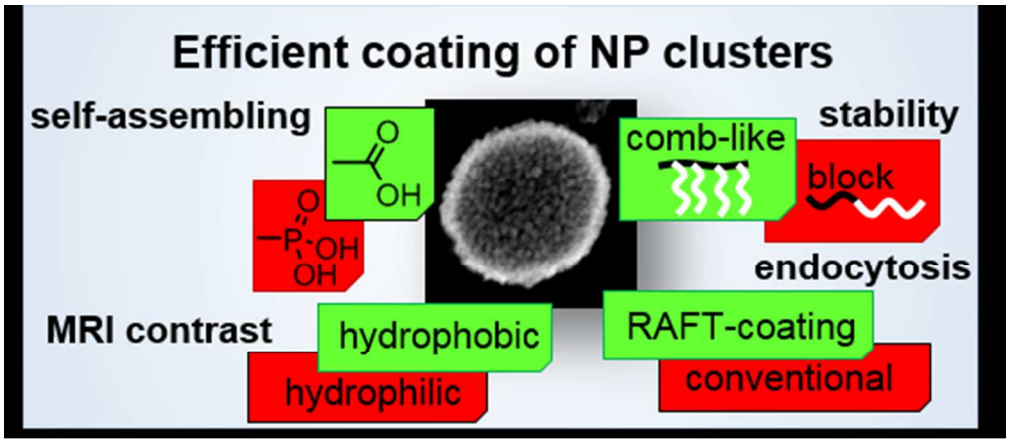
(61) Tanimoto, A. T.; Pouliquen, D.; Kreft, B. P.; Stark, D. D. Effects of Spatial Distribution on Proton Relaxation Enhancement by Particulate Iron Oxide. *J. Magn. Reson. Imaging* **1994**, *4*, 653-657.

(62) Weiswald, L.-B.; Bellet, D.; Dangles-Marie, V. Spherical Cancer Models in Tumor Biology. *Neoplasia* **2015**, *17*, 1-15.

(63) Fennema, E.; Rivron, N.; Rouwkema, J.; van Blitterswijk, C.; de Boer, J. Spheroid Culture as A Tool for Creating 3D Complex Tissues. *Trends Biotechnol.* **2012**, *31*, 108-115.

(64) Levy, M. L., F.; Maraloiu, V. A.; Blanchin, M. G.; Gendron, F.; Wilhelm, C.; Gazeau, F. Degradability of Superparamagnetic Nanoparticles in a Model of Intracellular Environment: Follow-up of Magnetic, Structural and Chemical Properties. *Nanotechnology* **2010**, *21*, 395103-395200.

(65) Reynolds, L.; Gardecki, J. A.; Frankland, S. J. V.; Horng, M. L.; Maroncelli, M. Dipole Solvation in Nondipolar Solvents: Experimental Studies of Reorganization Energies and Solvation Dynamics. *J. Phys. Chem. C* **1996**, *100*, 10337-10354.



94x40mm (150 x 150 DPI)